The Astrophysical Journal, 971:185 (23pp), 2024 August 20 https://doi.org/10.3847/1538-4357/ad5541

© 2024. The Author(s). Published by the American Astronomical Society.

OPEN ACCESS

Ubiquitous Late Radio Emission from Tidal Disruption Events

Y. Cendes[1,2], E. Berger[1], K. D. Alexander[3], R. Chornock[4], R. Margutti[4,5], B. Metzger[6,7], M. H. Wieringa[8], M. F. Bietenholz[9], A. Hajela[10], T. Laskar[11,12], M. C. Stroh[13], and G. Terreran[14]
[1] Center for Astrophysics, Harvard & Smithsonian, Cambridge, MA 02138, USA; yncendes@uoregon.edu
[2] Department of Physics, University of Oregon, Eugene, OR 97403, USA
[3] Department of Astronomy and Steward Observatory, University of Arizona, 933 North Cherry Avenue, Tucson, AZ 85721-0065, USA
[4] Department of Astronomy, University of California, Berkeley, CA 94720-3411, USA
[5] Department of Physics, University of California, 366 Physics North MC 7300, Berkeley, CA 94720, USA
[6] Department of Physics and Columbia Astrophysics Laboratory, Columbia University, Pupin Hall, New York, NY 10027, USA
[7] Center for Computational Astrophysics, Flatiron Institute, 162 5th Avenue, New York, NY 10010, USA
[8] CSIRO Space and Astronomy, P.O. Box 76, Epping NSW 1710, Australia
[9] Department of Physics and Astronomy, York University, 4700 Keele Street, Toronto, Ontario M3J 1P3, Canada
[10] DARK, Niels Bohr Institute, University of Copenhagen, Jagtvej 128, DK-2200 Copenhagen, Denmark
[11] Department of Physics & Astronomy, University of Utah, Salt Lake City, UT 84112, USA
[12] Department of Astrophysics/IMAPP, Radboud University, P.O. Box 9010, 6500 GL, The Netherlands
[13] Center for Interdisciplinary Exploration and Research in Astrophysics (CIERA) and Department of Physics and Astronomy, Northwestern University, Evanston, IL 60208, USA
[14] Las Cumbres Observatory, 6740 Cortona Drive, Suite 102, Goleta, CA 93117-5575, USA

Received 2023 August 25; revised 2024 May 29; accepted 2024 May 29; published 2024 August 20

Abstract

We present radio observations of 23 optically discovered tidal disruption events (TDEs) on timescales of ∼500–3200 days postdiscovery. We detect nine new TDEs that did not have detectable radio emission at earlier times, indicating a late-time brightening after several hundred (and up to 2300) days; an additional seven TDEs exhibit radio emission whose origin is ambiguous or may be attributed to the host galaxy or an active galactic nucleus. We also report a new rising component in one TDE previously detected in the radio at $\sim 10^3$ days. While the radio emission in some of the detected TDEs peaked on a timescale ≈2–4 yr, over half of the sample still show rising emission. The range of luminosities for the sample is $\sim 10^{37}$–10^{39} erg s^{-1}, about 2 orders of magnitude below the radio luminosity of the relativistic TDE Sw J1644+57. Our data set indicates ∼40% of all optical TDEs are detected in radio hundreds to thousands of days after discovery, and that this is probably more common than early radio emission peaking at $\sim 10^2$ days. Using an equipartition analysis, we find evidence for a delayed launch of the radio-emitting outflows, with delay timescales of ∼500–2000 days, inferred velocities of ≈0.02–0.15c, and kinetic energies of $\sim 10^{47}$–10^{49} erg. We rule out off-axis relativistic jets as a viable explanation for this population, and conclude delayed outflows are a more likely explanation, possibly from delayed disk formation. We conclude late radio emission marks a fairly ubiquitous but heretofore overlooked phase of TDE evolution.

Unified Astronomy Thesaurus concepts: Black holes (162); Tidal disruption (1696); Radio astronomy (1338)

Materials only available in the online version of record: machine-readable tables

1. Introduction

Optical/UV and X-ray emissions from tidal disruption events (TDEs) are generally thought to track the mass fallback (e.g., Guillochon & Ramirez-Ruiz 2013; Stone et al. 2013) and cooling (e.g., Metzger 2022) of bound stellar debris onto a central supermassive black hole. Radio observations, on the other hand, can reveal and characterize outflows from TDEs (Alexander et al. 2020), including the presence of relativistic jets (e.g., Giannios & Metzger 2011; Zauderer et al. 2011; De Colle et al. 2012; Andreoni et al. 2022).

To date, rapid follow-up of TDEs within the first days to weeks after discovery has led to the radio detection of several events. These include most prominently Swift J1644+57 (Sw J1644+57), whose radio and millimeter emission are powered by a relativistic outflow with an energy of $\sim 10^{52}$ erg and an initial Lorentz factor of $\Gamma \sim 10$, first detected in radio ∼2 days after its initial discovery in gamma rays (Zauderer et al. 2011, 2013; Berger et al. 2012; Metzger et al. 2012; Eftekhari et al. 2018; Cendes et al. 2021b). Other events, such as ASASSN-14li and AT2019dsg, have instead exhibited evidence for nonrelativistic outflows, with $E_K \sim 10^{48}$–10^{49} erg and $\beta \approx 0.05$–0.1, with first radio detections within a few weeks of discovery (e.g., Alexander et al. 2016, 2020; Pasham & van Velzen 2018; Cendes et al. 2021a; Stein et al. 2021).

Currently, most studies of radio TDEs primarily focus on the detection of radio emission at time in days $t_d < 100$ days, and emission is detected in ∼20%–30% of cases (Alexander et al. 2020). Recently, however, four TDEs have been reported to show radio emission with a delay relative to the time of optical discovery.[15] AT2018hyz was first detected at ∼1000 days postdiscovery, despite several constraining upper limits at earlier times (including at 705 days), and has been increasing at a steep rise of $F_\nu \propto t^5$ relative to the time of optical discovery (Cendes et al. 2022b). This delay and rapid rise have been interpreted as either due to a delayed, mildly relativistic outflow

Original content from this work may be used under the terms of the Creative Commons Attribution 4.0 licence. Any further distribution of this work must maintain attribution to the author(s) and the title of the work, journal citation and DOI.

---

[15] IGRJ12580 is an X-ray-discovered possible TDE with a delayed radio flare (Perlman et al. 2022), but is outside the scope of this paper, which is focused on optically selected TDEs.

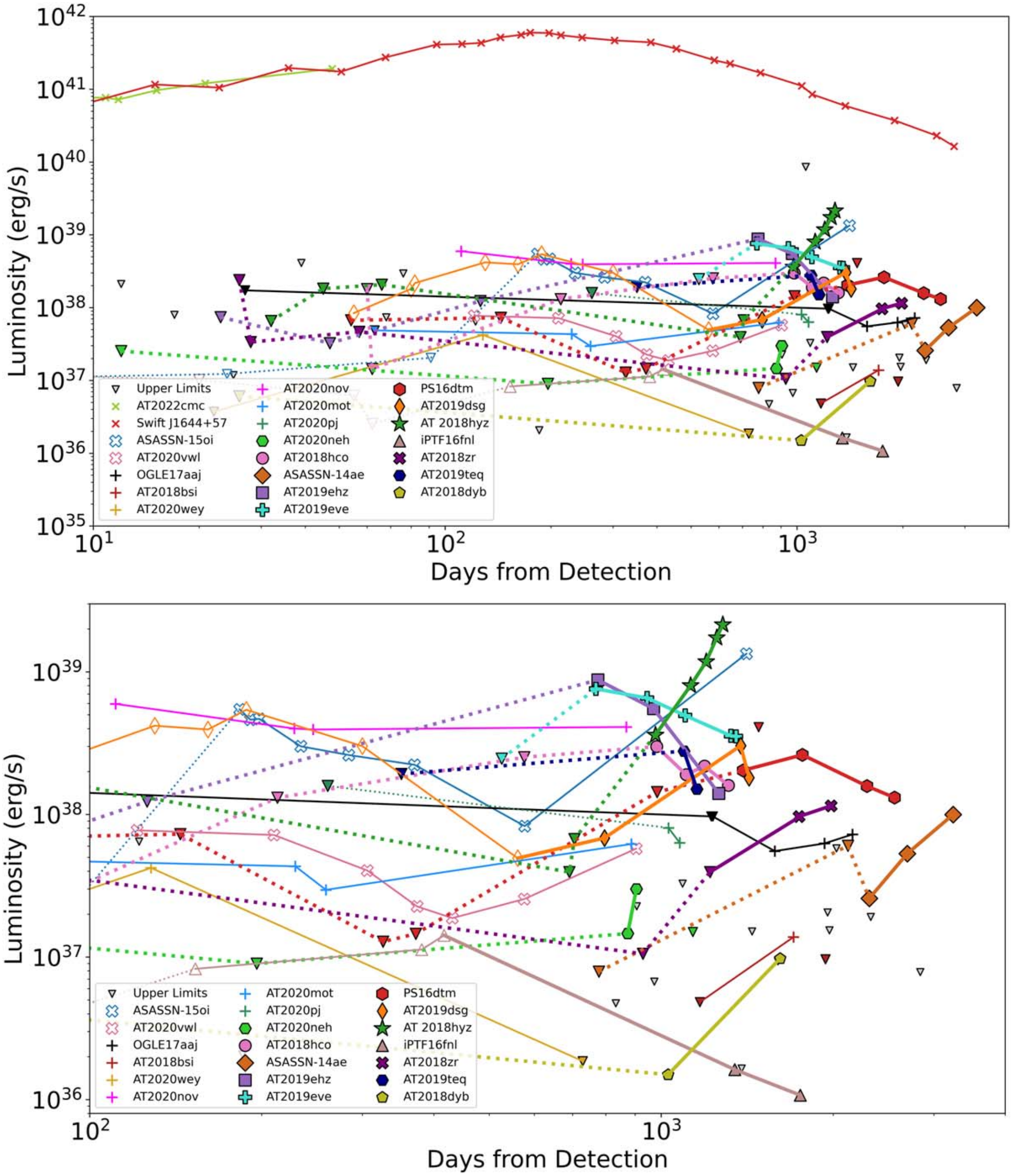

Figure 1. Top: radio luminosity light curves for the TDEs presented in this work (triangles: 3σ upper limits; other symbols: detections). All observations for the same TDE are connected with a dotted line for nondetections, and a solid line when detected. TDEs with detected radio emission whose origin is ambiguous are shown as plus symbols (see Section 3.1.3). We also include the light curve for AT2018hyz from Cendes et al. (2022b). For comparison we also show radio light curves for TDEs with early jetted radio emission (Sw J1644+57: Cendes et al. 2021b; AT2022cmc: Andreoni et al. 2022) and TDEs with late brightening (ASASSN-15oi: Horesh et al. 2021a; AT2020vwl: Goodwin et al. 2023a, 2023b) as well as one TDE with early radio emission for which we detect significant rebrightening (Cendes et al. 2021a; Stein et al. 2021), where previously published data are shown as open symbols, and our new data are shown with filled symbols connected by thicker lines. We do not plot nonconstraining upper limits, but they are available in Table 5 in the Appendix. Bottom: the same data presented above, but zoomed in to only show observations at >100 days, and luminosities of $<3 \times 10^{39}$ erg s^{-1}, highlighting the significant population of TDEs with late-rising radio emission.

launched ≈750 days after optical discovery, or an off-axis jet which was launched promptly at the time of optical discovery and whose emitting area and angle have increased over time (Cendes et al. 2022b; Matsumoto & Piran 2023). ASASSN-15oi was first detected ≈180 days after optical discovery with a luminosity that exceeded earlier radio limits by a factor of ≈20 (Horesh et al. 2021a); this emission subsequently declined until about 550 days, and then exhibited a second rapid rise with a detection at 1400 days with an even higher luminosity than the first peak; see Figure 1. iPTF16fnl was first detected ≈150 days after optical discovery, with a luminosity about a factor of 8 times larger than earlier limits (extending to 63 days) and appeared to slowly brighten to about 417 days (Horesh et al. 2021b). The initial abrupt rise in ASASSN-15oi seems to differ from the radio light curve of AT2019dsg, although both reach their peak radio luminosity on a similar timescale and at a

Table 1
Tidal Disruption Events Studied in This Work

Object	z	Distance (Mpc)	Discovery Date (UT)	TDE Class	Discovery Paper
TDEs with Previously Known Radio Emission					
iPTF16fnl	0.0163	71	2016 Aug 29	TDE-H+He	Blagorodnova et al. (2017)
AT2019dsg	0.0512	230	2019 Apr 9	TDE-H+He	Hammerstein et al. (2023)
AT2020mot[a]	0.070	317	2020 Jun 14	TDE-H+He	Hammerstein et al. (2023)
TDEs with Newly Detected Radio Emission					
ASASSN-14ae	0.0436	200	2014 Jan 25	TDE-H+He[b]	Holoien et al. (2014)
PS16dtm	0.0804	368	2016 Aug 12	TDE-H	Blanchard et al. (2017)
OGLE17aaj[a]	0.116	540	2017 Jan 2	TDE-H+He	Gromadzki et al. (2019)
AT2018zr	0.071	323	2018 Mar 2	TDE-H+He[b]	van Velzen et al. (2021)
AT2018dyb	0.018	79	2018 Jul 11	TDE-Bowen	Holoien et al. (2020)
AT2018bsi[a]	0.051	228	2018 Apr 9	TDE-H+He	van Velzen et al. (2021)
AT2018hco	0.088	404	2018 Oct 4	TDE-H	van Velzen et al. (2021)
AT2018hyz	0.046	205	2018 Oct 14	TDE-H+He[b]	Gomez et al. (2020), Short et al. (2020)
AT2019ehz	0.074	338	2019 Apr 29	TDE-H	van Velzen et al. (2021)
AT2019eve	0.081	372	2019 May 5	TDE-H	van Velzen et al. (2021)
AT2019teq	0.087	404	2019 Oct 20	TDE-H+He	Hammerstein et al. (2023)
AT2020nov[a]	0.084	385	2020 Jun 27	TDE-H+He	Frederick et al. (2020)
AT2020neh	0.062	280	2020 Jun 19	TDE-H+He	Angus et al. (2022)
AT2020pj[a]	0.068	308	2020 Jan 2	TDE-H+He	Hammerstein et al. (2023)
AT2020wey[a]	0.027	120	2020 Oct 8	TDE-H+He	Hammerstein et al. (2023)
TDEs with No Detected Radio Emission					
DES14C1kia	0.162	782	2014 Nov 11	TDE-He	Foley et al. (2015)
iPTF15af	0.079	360	2015 Jan 15	TDE-H+He	Blagorodnova et al. (2019)
iPTF16axa	0.108	503	2016 May 29	TDE-H+He	Hung et al. (2017)
AT2017eqx	0.109	508	2017 Jun 7	TDE-H+He	Nicholl et al. (2019)
AT2018fyk	0.059	264	2018 Sept 8	TDE-H+He	Wevers et al. (2019)
AT2018lna	0.091	419	2018 Dec 28	TDE-H+He	van Velzen et al. (2021)

Notes. For this table and throughout this paper we assume a flat Lambda cold dark matter (ΛCDM) cosmology with $H_0 = 69.6$ km s^{-1} Mpc^{-1}, $\Omega_m = 0.286$, and $\Omega_\Lambda = 0.714$ (Wright 2006).

[a] TDEs for which radio emission was detected in our observations, but the nature of the emission is ambiguous, or due to star formation or an active galactic nucleus (AGN; see Section 3.1.3).

[b] These TDEs showed only H lines in their initial classification spectra, leading to their labeling as TDE-H in some references. However, Holoien et al. (2014) report the emergence of He II in ASASSN-14ae in later epochs, which eventually becomes stronger than the H Balmer lines. Similarly, although AT2018hyz was classified by van Velzen et al. (2021) as a TDE-H, Short et al. (2020) report the presence of both He I and He II emission lines (the latter appearing at ∼70–100 days). AT2018zr had the most delayed appearance of He II emission, at ≈170 days postdiscovery (Hung et al. 2019). We therefore list all three objects as TDE-H+He.

similar level. The gradual rise and much lower peak luminosity of iPTF16fnl (≈10^{37} erg s^{-1}), on the other hand, may indicate that it is simply a less energetic example of typical radio-emitting TDEs. Finally, it is possible that TDEs with prompt detections can exhibit a secondary rebrightening after emission has faded; in the case of AT2020vwl, which was first detected in radio ∼120 days postdisruption, the source declined in emission to ∼430 days and is now increasing in brightness 900 days post–optical discovery (Goodwin et al. 2023a, 2023b).

Here, we present radio observations of a sample of 23 optically detected TDEs on a timescale of about 500–2500 days postdisruption, which show ∼40% of these TDEs have radio detections at these late times despite no emission detected at earlier times. Our extensive multifrequency data allow us to present detailed physical parameters for this TDE population in energetics, densities, and luminosities. This more than doubles the number of radio-detected TDEs to date, and allows us to show an increasing diversity in the TDE landscape, particularly at these later timescales.

Our paper is structured as follows. In Section 2, we present our radio observations. In Section 3, we discuss our results for individual TDEs in our study, including radio luminosity and evolution for individual TDEs and the rate of late-time TDE radio emission. In Section 4 we discuss equipartition analysis for TDEs where multifrequency data are available and estimated launch dates of the radio outflows. In Section 5 we discuss our findings in the context of the TDE population, with additional analysis presented in an upcoming companion paper. We summarize our conclusions in Section 6.

2. Sample Selection and Observations

We observed 24 optically selected TDEs, extending to $z \approx 0.16$, discovered between 2014 January and 2020 October. The targets were drawn from the samples of van Velzen et al. (2020) and Hammerstein et al. (2023), supplemented with a few additional events from the literature. The sample of events is presented in Table 1. All TDEs were 2–6 yr postdiscovery at the time of our observations. We emphasize that one of these TDEs, AT2018hyz, showed an especially dramatic radio brightening starting at ≈3 yr post–optical discovery and was presented in detail in a previous paper (Cendes et al. 2022b).

The properties of all 24 TDEs in our sample are provided in Table 5 in the Appendix.

We obtained radio observations with the Karl G. Jansky Very Large Array (VLA), the MeerKAT radio telescope, and the Australian Telescope Compact Array (ATCA). VLA observations were first obtained in *C* band (6 GHz), followed by multifrequency observation in *L* to *K* bands (1–26 GHz) in the event of a detection (program IDs: 20A-492, PI: Alexander; 21A-303, PI: Hajela; 21B-360, PI: Cendes; and 22B-205, PI: Cendes). We processed the data using standard data reduction procedures in the Common Astronomy Software Application package (McMullin et al. 2007), using `tclean` on the calibrated measurement sets available in the NRAO archive. We obtained all flux densities and uncertainties using the `imtool fitsrc` command within the `pwkit` package (Williams et al. 2017).[16] We assumed a point-source fit, as preferred by the data. The resulting flux density measurements are provided in Table 5 in the Appendix.

We obtained MeerKAT observations in *L* band (1.36 GHz) and *U* band (0.88 GHz; program IDs: DDT-20200911-YC-01, PI: Cendes; SCI-20210212-YC-01, PI: Cendes; DDT-20220414-YC-01, PI: Cendes; SCI-20220822-YC-01, PI: Cendes; and SCI-20220822-MB-03, PI: Bietenholz). We used the standard calibrated MeerKAT pipeline images available via the SARAO Science Data Processor (SDP),[17] with the exception of data from SCI-20220822-MB-03, which was processed by `OxKAT` (Heywood 2020). We confirmed via the secondary SDP products that the other sources in the MeerKAT images also in the NRAO VLA Sky Survey (Condon et al. 1998) were within ∼10% in expected flux. We then obtained all flux densities and uncertainties using the `imtool fitsrc` command within `pwkit`. The resulting flux density measurements are provided in Table 5 in the Appendix.

We obtained ATCA observations in *S* to *Ku* band (2–20 GHz; program IDs: C3472, PI: Cendes; and C3325, PI: Alexander). We analyzed the data using the `MIRIAD` package with the respective calibrators for absolute flux density and bandpass, and to correct short-term gain and phase changes. The `invert`, `mfclean`, and `restor` tasks were used to make deconvolved wide-band, natural-weighted images in each frequency band. Flux densities were determined by fitting a point-source model using the `Miriad imfit` tasks; for any upper limits, the image value at the expected location was used. The resulting flux density measurements are provided in Table 5 in the Appendix.

Additionally, we obtained archival images from the Very Large Array Sky Survey (VLASS; Lacy et al. 2020), and from the Variables and Slow Transients Survey (VAST; Murphy et al. 2021) where available; the VLASS images are taken in *S* band (3 GHz) and the VAST images in UHF band (0.88 GHz). We measured the flux densities in these images with the `imtool fitsrc` command within `pwkit`. We also checked the NRAO data archive, MeerKAT data archive, and the Australia Telescope National Facility data archives and included any unpublished observations of our TDE sample, with the relevant project codes listed in Table 5 in the Appendix.

For all TDEs, we define the times of our observations relative to the date of the TDE discovery (δt). In the case of a nondetection, we report a 3σ upper limit. We note that the uncertainties listed in Table 5 in the Appendix are statistical only and do not include an expected ≈3%–5% systematic uncertainty in the overall flux density calibration; we account for this systematic uncertainty in our subsequent modeling (Section 4).

3. Results

3.1. Radio Luminosity and Time Evolution

Of the 24 TDEs in our full sample (including AT2018hyz), 17 are detected in our observations on a timescale of ≈770–3250 days. A detailed description of each TDE is provided in Section 3.1.1. Of the 17 detected TDEs, three were detected in the radio at earlier times: iPTF16fnl (Horesh et al. 2021b), AT2019dsg (Cendes et al. 2022b), and AT2020mot (Liodakis et al. 2023). Additionally, in six of the 17 detected TDEs the nature of the radio emission is ambiguous, namely they do not exhibit significant time evolution and/or lack constraining early limits; the radio emission in these cases may be due to a preexisting AGN or star formation in the host galaxy. This leaves 10 TDEs with definitive late-time radio emission well in excess of nondetections at early times (including AT2018hyz), requiring significant brightening hundreds of days post–optical discovery.

We present the radio light curves for all 24 sources in this full sample, including upper limits, in Figure 1. For the purpose of comparison, we also include the radio light curves of the jetted TDEs Sw J1644+57 (Eftekhari et al. 2018; Cendes et al. 2021b) and AT2022cmc (Andreoni et al. 2022), and two previous TDEs with late radio emission, ASASSN-15oi (Horesh et al. 2021a) and AT2020vwl (Goodwin et al. 2023a, 2023b). We also include previously published data for iPTF16fnl (Blagorodnova et al. 2017; Horesh et al. 2021b), AT2018dyb (Holoien et al. 2020), iPTF15af (Blagorodnova et al. 2019), PS16dtm (Blanchard et al. 2017), AT2018hco (Horesh et al. 2018), AT2020mot (Liodakis et al. 2023), AT2018hyz (Cendes et al. 2022b), and AT2019dsg (Cendes et al. 2021a; Stein et al. 2021). In all cases where multifrequency observations are available, we use data in *C* band (6 GHz).

3.1.1. Tidal Disruption Events with Newly Discovered Late Radio Emission

We report nine new TDEs with late-time radio emission identified based on our observations and constraining earlier nondetections (from targeted or survey data). These light curves can be seen in Figure 2. Below we briefly describe the radio light-curve properties of each event.

1. ASASSN-14ae was optically discovered on 2014 January 25 at a redshift of $z = 0.0436$ (Holoien et al. 2014), making it the oldest TDE in our sample. A VLA observation at 778 days yielded an upper limit of $\lesssim 0.033$ mJy at 6 GHz, and a VLASS observation at 2122 days yielded an upper limit of $\lesssim 0.42$ mJy at 3 GHz. We first detected ASASSN-14ae at 2313 days when it was 0.090 ± 0.015 mJy at 6 GHz, and found a steady (and ongoing) rise in its light curve over subsequent observations to 0.42 ± 0.08 mJy at 3243 days, or a luminosity of 1×10^{38} erg s^{-1}. This corresponds with a factor of ∼4 increase in luminosity since detection, with a steep power-law rise since initial detection of ($F_\nu \propto t^\alpha$) with

---

[16] https://github.com/pkgw/pwkit

[17] https://skaafrica.atlassian.net/wiki/spaces/ESDKB/pages/338723406/

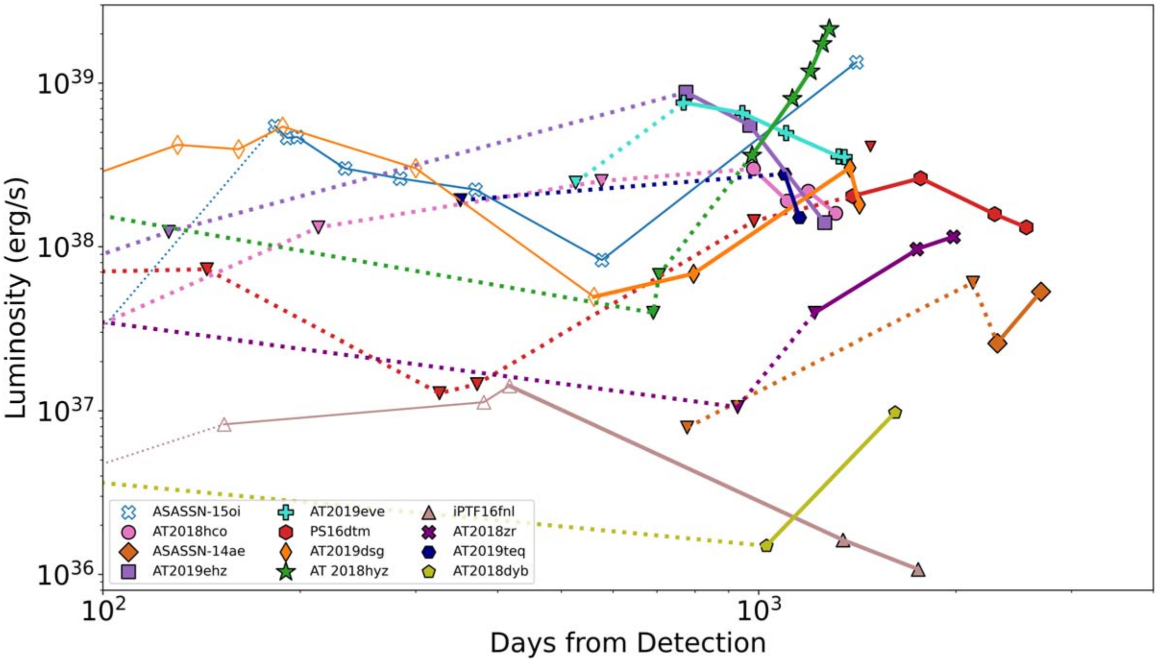

Figure 2. As in the bottom of Figure 1, but only for the main sources listed in Sections 3.1.1 and 3.1.2.

$\alpha = 4.2$. Continued observations of the rising light curve are ongoing.

2. PS16dtm was optically discovered on 2016 August 12 at a redshift of $z = 0.0804$ (Blanchard et al. 2017; Jiang et al. 2017; Petrushevska et al. 2023). Four radio observations in approximately the first year resulted in nondetections, with the first nondetection at 54 days and the latest nondetection at 372 days, when it was $\lesssim 0.015$ mJy at 6 GHz (Blanchard et al. 2017). It should be noted that PS16dtm had a preexisting AGN; however with several nondetections in radio it is expected that the AGN contribution to the radio emission was minimal (Blanchard et al. 2017). We first detected PS16dtm at 1391 days with 0.210 ± 0.008 mJy at 6 GHz (2.0×10^{38} erg s^{-1}). The light curve rose to a peak of 0.271 ± 0.002 mJy (2.6×10^{38} erg s^{-1}) at 1767 days, and faded to 0.163 ± 0.012 mJy (1.6×10^{38} erg s^{-1}) by 2291 days.
3. AT2018zr (also known as PS18kh) was discovered optically on 2018 March 2 at $z = 0.075$ (Hung et al. 2019). Initial observations with the Arcminute Microkelvin Imager (AMI) at 16 GHz and the VLA at 10 GHz at 26–57 days yielded no detections (van Velzen et al. 2019); observations from our program at 929 and 1218 days at 6 GHz yielded upper limits of <0.014 and <0.053 mJy, respectively. The source was then detected at 1713 days, with 0.147 ± 0.011 mJy at 6 GHz, and had risen to 0.155 ± 0.018 mJy 30 days later. This corresponds to a rise in luminosity of $\gtrsim 2.5\times$ from the last upper limit ($\lesssim 3.9 \times 10^{37}$ erg s^{-1} to 9.7×10^{37} erg s^{-1}), corresponding to a power-law index of $\alpha \gtrsim 2.7$ from its last upper limit to first detection. The TDE was at peak luminosity in our last observation, and future observations will allow us to determine the evolution of this TDE.
4. AT2019teq was optically discovered on 2019 October 20 at $z = 0.087$ (Hammerstein et al. 2023). Yao et al. (2023) reported an X-ray brightening and hardening of this TDE on 2022 September 8 (1050 days), which was confirmed by NICER observations on 2022 October 18–21 (1100 days). No prior radio observations of AT2019teq exist except for a VLASS observation at 351 days with an upper limit of <0.33 mJy at 3 GHz. Our VLA observation at 1096 days at 6 GHz resulted in a detection with 0.238 ± 0.008 mJy (Cendes et al. 2022a), and the emission subsequently faded at 1155 days to 0.129 ± 0.016 mJy. Given the decline between our two observations, and the earlier nondetection, we conclude that the radio emission peaked at $\sim$400–1000 days; the lower limit on the peak radio luminosity is $\approx 2.7 \times 10^{38}$ erg s^{-1}.
5. AT2018dyb (ASASSN-18pg) was optically discovered on 2018 July 11, at $z = 0.018$ (Leloudas et al. 2019; Holoien et al. 2020). Radio observations at 26 days led to an upper limit of <0.43 mJy at 19 GHz. Our first observation took place at 1028 days and led to a detection with 0.158 ± 0.06 mJy at 1.3 GHz. The emission then dramatically brightened at 1615 days to 1.03 ± 0.07 mJy ($\approx 10^{37}$ erg s^{-1}), corresponding to a power-law index of $\alpha \approx 4.2$ since its first detection. Future observations will allow us to determine the evolution of this TDE.
6. AT2018hco was optically discovered on 2018 October 4 at $z = 0.088$ (van Velzen et al. 2020). Radio nondetections were obtained with AMI at 15.5 GHz at 60 days (<0.08 mJy; Horesh et al. 2018). We also identified a VLA archival observation at 62 days leading to a limit of <0.016 mJy at 6 GHz (18A-373, PI: van Velzen), a VLASS observation at 213 days with <0.30 mJy, and a limit of <1.986 mJy at 0.88 GHz with the ASKAP VAST survey. We first detected radio emission at 982 days with 0.343 ± 0.015 mJy at 6 GHz, or a luminosity of 4×10^{38} erg s^{-1}. The emission then fades in subsequent observations to 0.265 ± 0.014 mJy at 5 GHz at 1191 days, and we then see the source fading over time, to 0.200 ± 0.019 mJy at 5.5 GHz with ATCA on 1311 days

(1.6×10^{38} erg s^{-1}). We note the dip in luminosity at 1106 days is due to the use of VLASS observation at 3 GHz compared to 6 GHz for the other data points. The decline in luminosity from the first to the last detection has a power-law index of $\alpha \approx -1.8$. We estimate that the light-curve peak occurred at ≈220–980 days.

7. AT2019ehz was optically discovered on 2019 April 29 at $z = 0.074$ (van Velzen et al. 2021). We obtained early limits from unpublished archival VLA data at 23 and 47 days (19A-395, PI: van Velzen) with resulting limits of <0.06 and <0.26 mJy, respectively, at 9 GHz. There is also a VLASS nondetection at 126 days with <0.30 mJy. We first detected radio emission at 775 days, with 1.07 ± 0.003 mJy at 6 GHz, or a luminosity of 8.7×10^{38} erg s^{-1}. The emission subsequently faded in observations at 970 and 1262 days, to 0.205 ± 0.034 mJy, corresponding to a power-law decline of $\alpha \approx -3.4$. Since the emission is declining and the last upper limit before detection is at 126 days, we conclude that the light peak occurred at ~130–700 days. However, we note with the inferred steep decline in luminosity, it is more likely the peak was actually much closer to the time of first detection. This could have implications for the launch of the outflow; for example, if the time of the delayed launch was at ≈600 days the power-law index would be about −1. We discuss this further in Section 4.3.
8. AT2019eve was optically discovered on 2019 May 5 at $z = 0.081$ (van Velzen et al. 2021). A VLASS observation at 526 days yielded a nondetection of <0.50 mJy. We detected this source at 769 days with 0.766 ± 0.009 mJy at 6 GHz, or a luminosity of 7.6×10^{38} erg s^{-1}. Subsequent observations to 1353 days indicate steady fading to a final flux density of 0.711 ± 0.133 mJy. The power-law index for the rise between the last upper limit and first detection is $\alpha \gtrsim 3$, while for the decline it is $\alpha \approx -1.4$. The light-curve peak occurred at ≈530–770 days.
9. AT2020neh was optically detected on 2020 June 19 at $z = 0.062$ (Angus et al. 2022). Radio observations at 12 and 196 days led to nondetections with <0.018 mJy and <0.016 mJy, respectively, at 15 GHz (Angus et al. 2022). Our first detection is at 874 days with 0.026 ± 0.006 mJy at 6 GHz, followed about 30 days later by a rise to 0.053 ± 0.012 ($\approx 3 \times 10^{37}$ erg s^{-1}), or $\alpha \approx 20$. Despite the apparent rapid rise, the faintness of the emission precluded multifrequency observations. Future observations will allow us to determine the evolution of this TDE.

3.1.2. Tidal Disruption Evens with Previously Known Radio Emission

We identify a distinct late-time radio rebrightening in one TDE that exhibited early radio emission with fading behavior prior to our observations, and one TDE that was identified in the literature as a late-time radio TDE (Horesh et al. 2021b). We also include these light curves in Figure 2. Below we briefly describe the radio light-curve properties of each event.

1. iPTF16fnl was optically discovered on 2016 August 29 at $z = 0.0163$ (Blagorodnova et al. 2017). There were several radio nondetections at 2–62 days with $\lesssim$0.027–0.12 mJy at 15 GHz ($\lesssim 2.5 \times 10^{36}$–$1.2 \times 10^{37}$ erg s^{-1}), followed by detections at 15 GHz at 153–417 days, with a peak luminosity at 417 days of $\approx 1.4 \times 10^{37}$ erg s^{-1} (Horesh et al. 2021b). We observed iPTF16fnl at 1345 days at 6 GHz and found that the source had faded to 0.045 ± 0.001 mJy, $\approx 1.6 \times 10^{36}$ erg s^{-1}. Our subsequent observation at 1752 days shows the source has faded to 0.0295 ± 0.007 mJy at 6 GHz (1.1×10^{36} erg s^{-1}).
2. AT2019dsg was optically discovered on 2019 April 9 at $z = 0.051$ (van Velzen et al. 2020). Radio emission was first detected at 52 days, steadily rose to a peak at ≈200 days with a luminosity of $\approx 5.4 \times 10^{38}$ erg s^{-1}, and then steadily declined through 560 days, to $\approx 4.9 \times 10^{37}$ erg s^{-1} (Cendes et al. 2021a; Stein et al. 2021). Our new VLA observations at 796 days revealed a slight rebrightening, with $\approx 6.8 \times 10^{37}$ erg s^{-1} at 6 GHz; this is about an order of magnitude brighter than expected from a continued steady decline. A follow-up MeerKAT observation at 1378 days had a flux density of 0.384 ± 0.026 mJy at 1.36 GHz. Extrapolating to 6 GHz assuming the same spectral energy distribution (SED) as observed at 1170 days leads to an estimated flux density of ≈0.8 mJy ($\approx 3 \times 10^{38}$ erg s^{-1}), or a power-law index of $\alpha \approx 3$ during this time period. A final observation on 1437 days at 1.36 GHz indicated the source had faded to 0.180 ± 0.009 mJy, extrapolated to 6 GHz as ≈0.48 mJy ($\approx 2 \times 10^{38}$ erg s^{-1}). Thus, we conclude that AT2019dsg has evidence for a separate emission component than its initial peak; continued observations will delineate this TDE's time evolution.

3.1.3. Tidal Disruption Evens with Ambiguous or Host/Active Galactic Nucleus Radio Emission

We identify radio emission in an additional six TDEs, but we cannot definitively ascertain its nature, due to an absence of earlier deep upper limits or a lack of significant time evolution during our observations. We exclude these sources from subsequent detailed analysis of our TDE sample and treat them in Section 3.2 as upper limits. Below we provide relevant information for completeness; the radio data for these TDEs are provided in Table 6 in the Appendix.

1. OGLE17aaj was discovered on 2017 January 2 at $z = 0.116$ (Gromadzki et al. 2019). We detect this source for the first time with MeerKAT at 1581 days at 1.6 GHz, with a flux density of 0.19 ± 0.02 mJy. We have also identified observations of this source as part of the ASKAP VAST survey at 1.42 GHz at 1224 and 1231 days, but these lead to nonconstraining upper limits of $\lesssim$0.3 mJy (3σ). In subsequent observations with MeerKAT and ATCA at 2161 days we find that the radio emission remains fairly steady ($\alpha \propto 0.6$). This, combined with the lack of a constraining upper limit at earlier times, leads us to conclude that the radio emission from OGLE17aaj is unlikely to be related to the TDE.
2. AT2018bsi was optically discovered on 2018 April 9 at $z = 0.051$ (van Velzen et al. 2020). We first observed this source with the VLA at 1169 days at 6 GHz, and found an upper limit of $\lesssim$0.013 mJy. A subsequent observation at 1705 days led to a significant detection at 6 GHz, with 0.037 ± 0.005 mJy. We note that VLASS observations, on 2019 May 24 and 2021 October 26 respectively, were nonconstraining upper limits of <0.3 mJy. However, due to the faintness of the emission, we are presently unable to obtain multifrequency follow-up, and we therefore

classify the radio emission as ambiguous until additional observations can be taken.

3. AT2020pj was optically discovered on 2020 January 2 at $z = 0.068$ (Hammerstein et al. 2023). The first available radio observation was at 261 days from VLASS, leading to an upper limit of $\lesssim$0.465 mJy at 3 GHz. We subsequently detected the TDE at 6 GHz on 1030 days with a flux density of 0.118 ± 0.006 mJy, and on 1078 days with 0.093 ± 0.011 mJy. Due to the initial shallow upper limit, and the marginal variability we cannot determine if the radio emission is due to the TDE. Continued monitoring will help to ascertain the nature of this emission.
4. AT2020mot was optically discovered on 2020 June 14 at $z = 0.070$ (Liodakis et al. 2023). It was first observed at 67 days at 15 GHz, with an upper limit of <0.027 mJy (Liodakis et al. 2023), but was subsequently detected at 229 days with 0.060 ± 0.008 mJy and 259 days with 0.041 ± 0.008 mJy at 6 GHz by Liodakis et al. (2023), who concluded that the emission was likely due to star formation activity in the host galaxy. We detected the source at 887 days with 0.086 ± 0.008 mJy at 6 GHz, and conclude that the variations in flux are more consistent with an AGN than star formation activity, but likely unrelated to the TDE.
5. AT2020nov was optically discovered on 2020 June 27 at $z = 0.084$ (Frederick et al. 2020). Radio emission was first detected at 111 days at 15 GHz with a flux density of 0.224 ± 0.009 mJy (VLA program 20A-372, PI: Alexander), and the source had subsequent detections at 228 and 246 days at 6 GHz, when it was 0.376 ± 0.010 mJy and 0.370 ± 0.01 mJy, respectively. In our own program, we observed AT2020nov at $t_d = 869$ days at 6 GHz and found the source to be 0.39 ± 0.02 mJy, which is consistent with a steady luminosity at earlier times. Due to a lack of variability, we conclude this emission is likely due to non-TDE-related emission in the host galaxy, such as star formation.
6. AT2020wey was optically discovered on 2020 October 8 at $z = 0.027$ (Hammerstein et al. 2023). A radio observation 22 days postdiscovery had an upper limit of <0.014 mJy at 15 GHz, followed by a detection at 128 days at 6 GHz of 0.408 ± 0.081 mJy (VLA program 20A-372, PI: Alexander). Our program observed this source at 6 GHz at $t_d = 729$ days, and yielded a nondetection of <0.018 mJy. Due to the weak detection at 128 days, and a lack of follow-up detections, we cannot conclude the radio emission is due to the TDE. We will continue monitoring this TDE to ascertain the nature of this emission in the future.

3.2. The Incidence Rate and Properties of the Late-time Radio Emission

Our sample of TDEs with radio observations is the largest to date: we observed 24 optically selected TDEs (of which AT2018hyz was the subject of a separate paper: Cendes et al. 2022b). In this paper we identify nine new TDEs that had constraining radio upper limits at early times, and then exhibit brighter radio emission hundreds of days post–optical discovery; this excludes the six events with radio emission that is either ambiguous in origin or unlikely to be associated with the TDE (Section 3.1.3), and two events with prior radio emission (Section 3.1.2). Including AT2018hyz, this corresponds to a high detection fraction of $10/22$ or $\approx$45%. Alternatively, if we count distinct late-time brightening in AT2019dsg we obtain a detection fraction of $11/24$ or $\approx$45%. Thus, regardless of the exact accounting we conclude that about half of all optically selected TDEs exhibit radio emission that rises on timescales of hundreds of days. This high fraction is particularly striking when compared to the published statistics of early radio detections of optically selected TDEs ($\lesssim$200 days) of $\approx$30% (Alexander et al. 2020).

In Figure 3 we explore the turn-on and peak timescales of detected radio emission in the full TDE population with radio detections. The left panel of Figure 3 shows the timescale at which radio emission is first detected. We find a broad range of timescales, spanning from a few days to $\approx$2300 days. We note that some TDEs without current radio detections may yet turn on at even later timescales, as highlighted by the case of ASASSN-14ae with a first detection at $\approx$2300 days, and is still rising. The overall distribution of turn-on timescales appears to exhibit three groupings. First, at $\lesssim$20 days are the jetted TDEs (Sw J1644+57, Swift J2058.4+0516, and AT2022cmc), which are detected early due to the combination of rapid triggering and luminous radio emission from a relativistic jet, as well as the rapidly evolving AT2019qiz, which was detected in the radio at 8 days (Nicholl et al. 2020). Second, at $\approx$20–200 days we find eight TDEs[18]). Finally, identified here for the first time, we find that about half of all TDEs with radio emission are detected only at $\gtrsim$600 days, with a peak at $\sim 10^3$ days. We note that the gap at $\approx$200–600 days may be due to observing gaps, so it is possible that there is a more continuous distribution of turn-on times; however, it is clear that turn-on timescales of $\sim 10^3$ days are at least (or more) common than at $\sim 10^2$ days. We also show in the left panel of Figure 3 the distribution of timescales of the first radio observation of each TDE. We note that for about 40% of the TDEs, the first observation led to the first detection (e.g., ASASSN-14li and AT2019dsg; Alexander et al. 2016; Stein et al. 2021), and it is therefore likely that a first radio detection would have been possible even earlier; for the remaining TDEs there is at least one nondetection prior to the first detection.

While the turn-on timescale is informative, and clearly hints at a distinction between early ($\sim 10^2$ days) and late-rising ($\sim 10^3$ days) radio emission, the time of first detection is at least in part affected by any delays in the first observation. An additional relevant timescale is that of peak radio emission, shown in the right panel of Figure 3; we use the time of peak at $\sim$6 GHz for uniformity. We note that in some cases the radio light curve is already declining at the time of discovery so only an upper limit on the peak timescale is available; conversely, in other cases the emission is still rising in our latest observations leading to a lower limit on the peak timescale. We are also further limited by the various detection limits and event distances in the TDE population. We further note that for the three TDEs with a clear double-peaked structure (ASASSN-15oi, AT2020vwl, and AT2019dsg) we include both peaks in the distribution. The overall distribution is somewhat more uniform than the distribution of first detections, but we still note a bimodality, with peaks at $\sim$150 days and $\sim$1500 days

---

[18] We note that this grouping includes ASASSN-15oi with a first detection at 183 days and iPTF16fnl with a first detection at 153 days, which were referred to as "late" emission by Horesh et al. (2021a, 2021b), but which we clearly see here are more typical of TDEs with early radio emission, and are distinct from the population of TDEs with radio emission only at $\gtrsim 10^3$ days identified here.

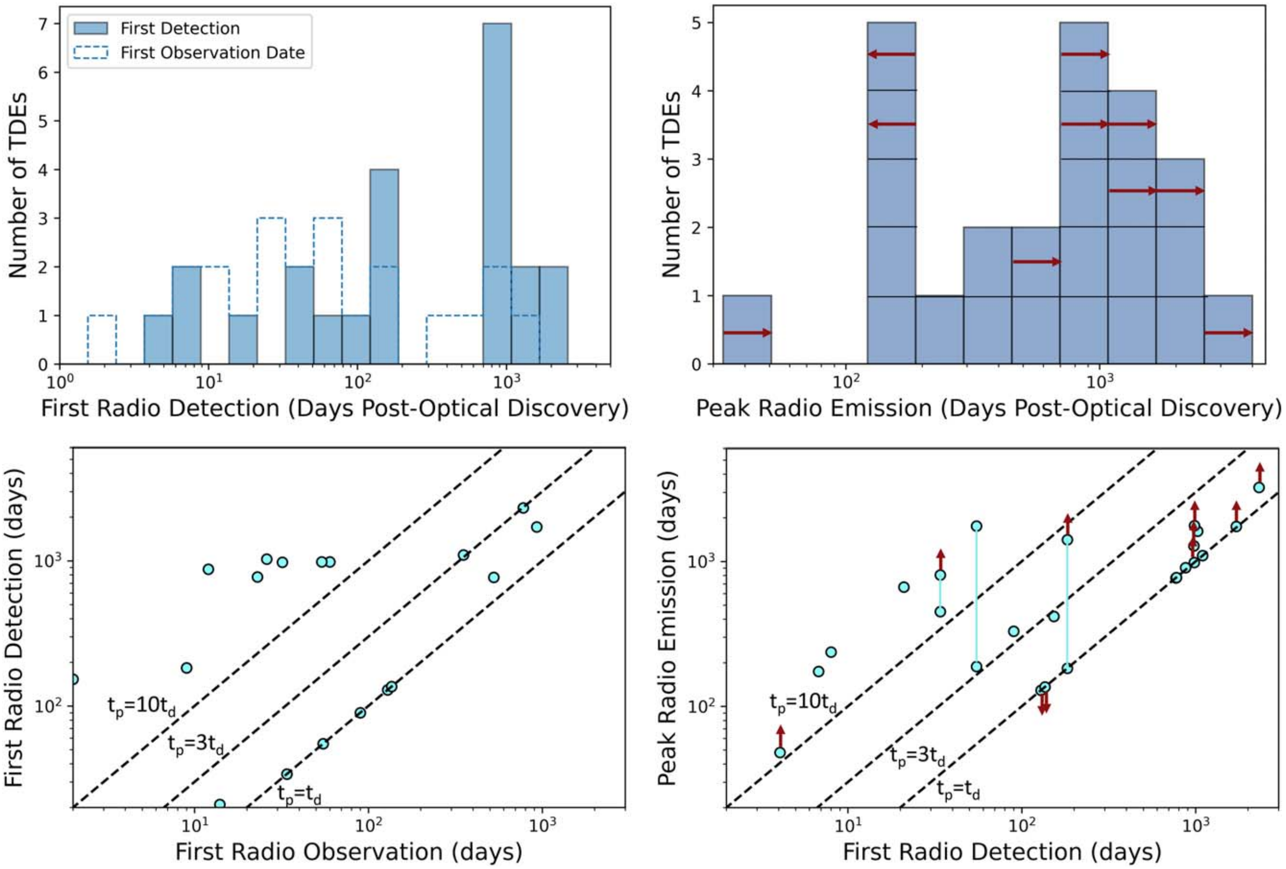

Figure 3. Upper left: histograms of the time of first radio detection (solid) and first radio observation (dashed) for TDEs with detected radio emission. Upper right: histogram of peak radio emission timescale at ∼6 GHz for TDEs with detected radio emission. Arrows indicate upper and lower limits. For TDEs with multiple distinct peaks (ASASSN-15oi and AT2019dsg), we include both components. Bottom left: the time of first radio observation vs. the time of first radio detection. The diagonal lines mark first radio detection, t_o, at multiples of 1, 3, and 10 times the time of first observation. Bottom right: time of peak radio emission vs. the time of first detection, with arrows indicating upper and lower limits; for the TDEs with distinct peaks (ASASSN-15oi, AT2019dsg, and AT2020vwl) we include both components connected by a solid line. The diagonal lines mark peak radio emission, t_p, at multiples of 1, 3, and 10 times the time of first detection. This indicates that for the TDE population with late radio emission at least some events may peak on a decade timescale. In addition to the data presented in this paper, radio data are from AT2019qiz (O'Brien et al. 2019; K. D. Alexander et al. 2024, in preparation), AT2019azh (Goodwin et al. 2022; Sfaradi et al. 2022), AT2019ahk (Christy et al. 2024), AT2019dsg (Cendes et al. 2021a; Stein et al. 2021), AT2020opy (Goodwin et al. 2023c), ASASSN-14li (Alexander et al. 2016), AT2020vwl (Goodwin et al. 2023a, 2023b), iPTF16fnl (Horesh et al. 2021b), and ASASSN-15oi (Horesh et al. 2021a). We also include the jetted TDEs AT2022cmc (Andreoni et al. 2022), Swift J1112.2-8238 (Brown et al. 2017), Swift J2058.4+0516 (Cenko et al. 2012), and Sw J1644+57 (Zauderer et al. 2011). We exclude TDEs in this plot where radio emission was ambiguous in nature (see Section 3.1.3).

(especially when we consider upper and lower limits). Regardless of the exact structure of the distribution, we find that ≈50% of TDEs with radio emission peak at $\gtrsim 10^3$ days. This is further highlighted in the bottom panel of Figure 3, where we plot the peak timescale versus the time of first detection, indicating that for events with early emission the peak emission timescale is typically ∼3–10 times higher than the time of first detection; while the events with first detections at $\sim 10^3$ days have mostly not reached their peak, if they had similar ratios they would peak on decade timescales.

Investigating the radio luminosities of the late emission, we find a range of $\approx 10^{37}$ to $\gtrsim 2 \times 10^{39}$ erg s^{-1}, but we stress that for several TDEs the emission is still rising, so both the lower and upper ranges may shift higher once all sources reach their peak. Overall, these radio luminosities are comparable to those of TDEs with early radio emission, but are ≈30–3000 times less luminous than Sw J1644+57 at a comparable timescale. We note that in the cases where the peak luminosity is well constrained by our detections and preceding upper limits (i.e., PS16dtm, AT2019eve, AT2019ezh, and AT2018hco) the peak luminosities are $\lesssim 10^{39}$ erg s^{-1}, compared to $\approx 10^{41}$ erg s^{-1} for Sw J1644+57, and it is therefore unlikely that their radio emission is due to initially off-axis jets; we return to this point in Section 5.2. On the other hand, the radio emission is still rising in some TDEs (i.e., ASASSN-14ae, AT2018dyb, AT2018zr, and AT2019dsg) although we note that those too currently have much lower luminosities than Sw J1644+57.

In Table 1 we include the TDE spectroscopic subclasses as outlined by van Velzen et al. (2020), namely TDE-H, TDE-H+He, and TDE-He. We find that all events in our sample classified as TDE-H exhibit delayed radio emission. We also find that we have two detections of TDE-H+He events (AT2019teq and AT2020neh), but the majority of our nondetections are of the TDE-H+He class. We will explore possible connections between the radio emission properties and the multiwavelength properties in a companion paper (K. D. Alexander et al. 2024, in preparation).

Finally, it is worth noting that the TDEs with no radio detections may in fact turn on at a later time than the observations presented here. For example, ASASSN-14ae is the oldest TDE in our sample and its first detection was at ≈2300 days. Regular monitoring of the TDE population is

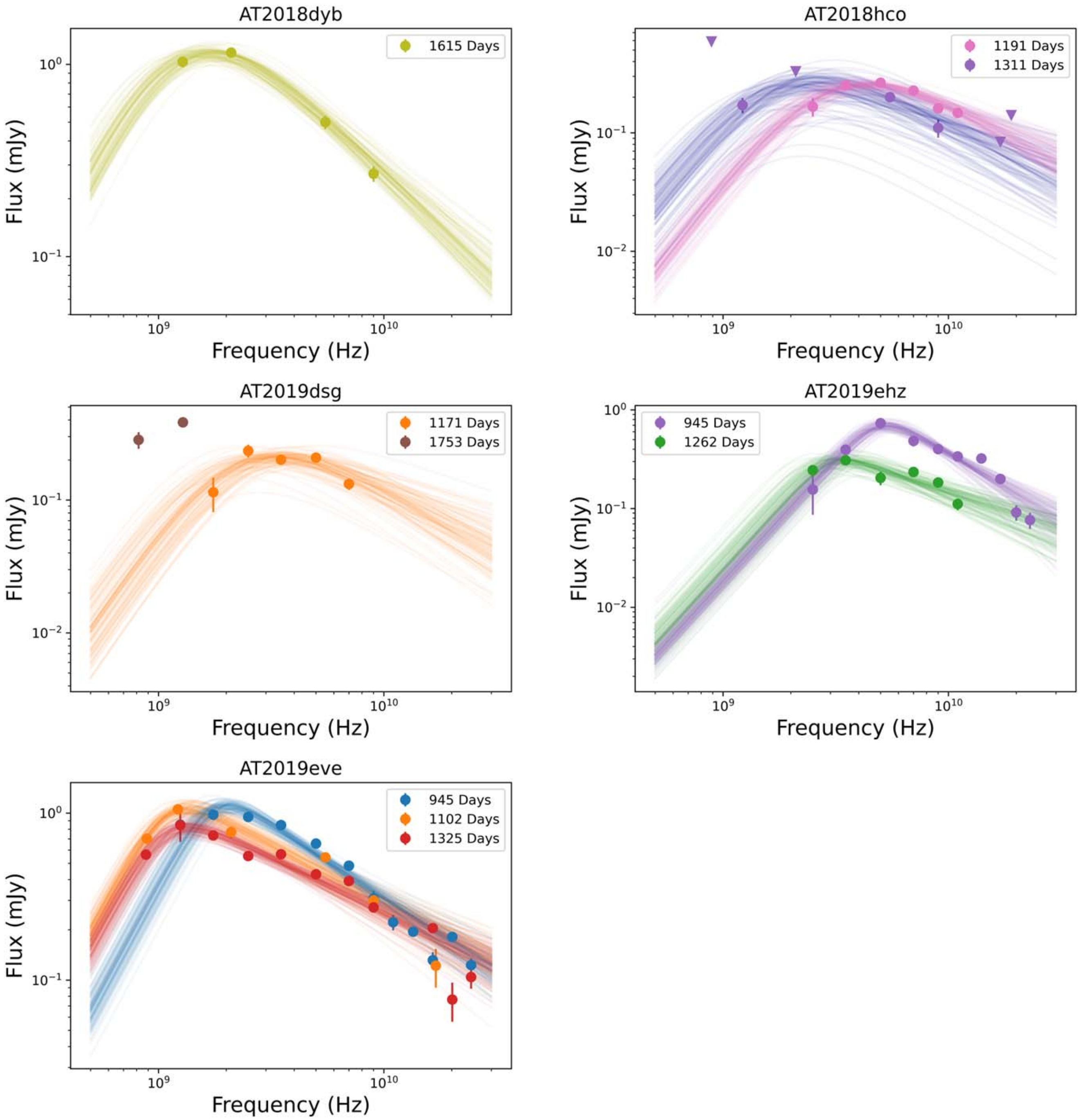

Figure 4. Radio SEDs for TDEs where ν_p is constrained. We denote upper limits as triangles, and do not include nonconstraining upper limits in these plots (they are available in Table 5 in the Appendix). The lines are representative fits from our Markov Chain Monte Carlo (MCMC) modeling of synchrotron self-absorbed spectra (Section 4).

crucial for determining the distribution of turn-on timescales; for example, in our own study, AT2018zr was not detected by two dedicated observations at 929 and 1218 days, but was then detected in a third observation at 1713 days. VLASS data were not constraining for this source, and without our prior deep upper limits it would have been difficult to constrain the timescale at which radio emission turned on.

4. Spectral Energy Distribution Modeling and Analysis

Beyond the light-curve data discussed in the previous section, we have also obtained multifrequency data for 10 TDEs with late-time radio emission,[19] allowing us to model their SEDs and extract physical properties of the outflows. The SEDs are characteristic of self-absorbed synchrotron emission, with (in some cases) a well-defined peak frequency (ν_p) and peak flux density ($F_{\nu,p}$), and a spectral shape of $F_\nu \propto \nu^{5/2}$ below ν_p (Figure 4). We chose this as the simplest explanation for the spectral shape, as other shapes (such as $F_\nu \propto \nu^2$) would

---

[19] We also obtained SEDs for OGLE17aaj and AT2020pj, but the origin of the radio emission in these sources is ambiguous (Section 3.1.3). We exclude these sources from our analysis, but provide the data for completeness in Table 6 in the Appendix.

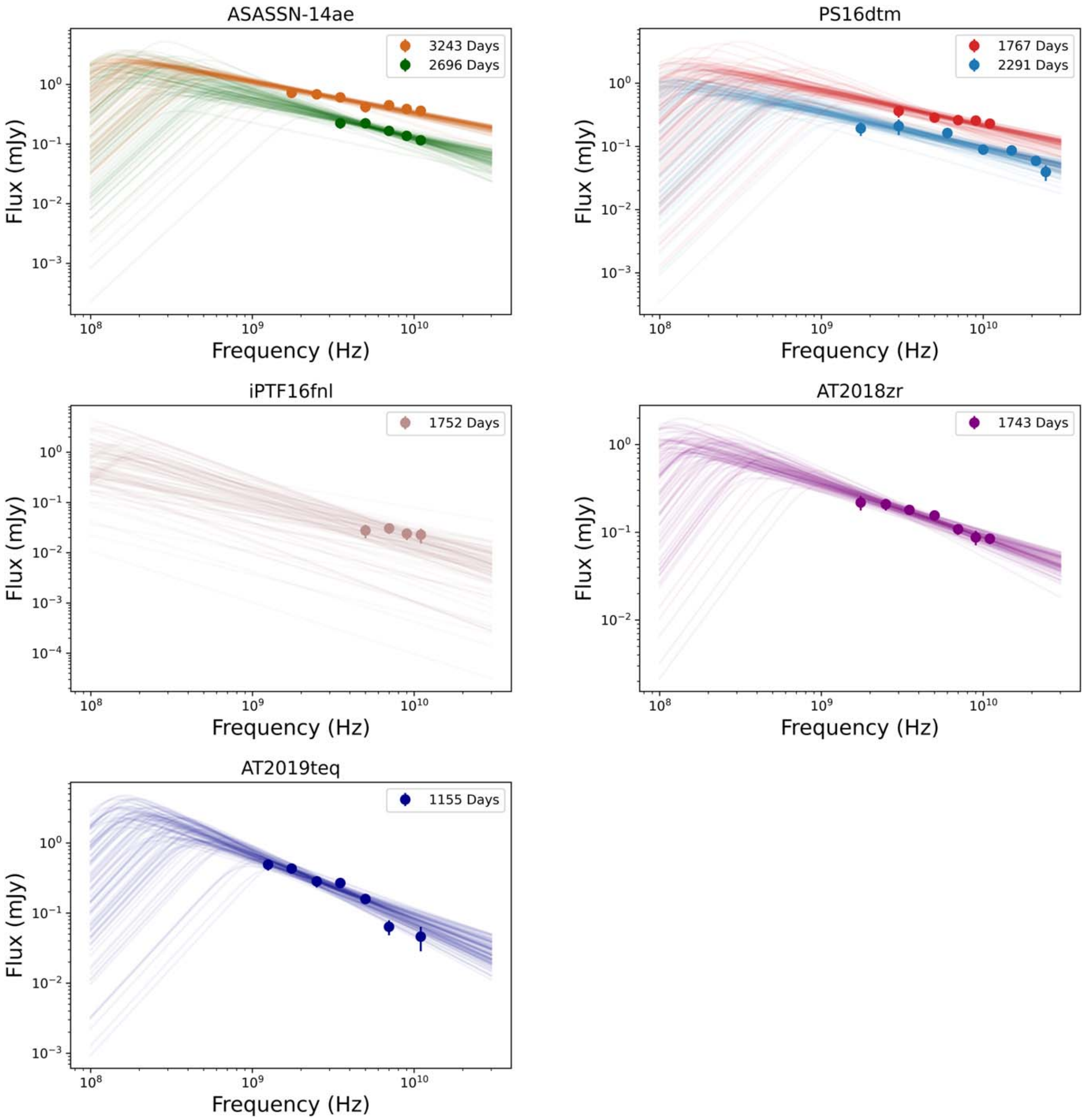

Figure 5. The same as Figure 4, but for TDEs where the SED is not constrained.

require a relativistic outflow, and this does not seem to be the case for the majority of TDEs (Alexander et al. 2020).[20] In several cases we find that the SED peak is below our lowest available frequency; we assume a self-absorbed synchrotron emission for these cases as well, and use the lowest-frequency data point as an upper limit on ν_p and a lower limit on $F_{\nu,p}$ (Figure 5). For six TDEs, we have two or three epochs of multifrequency observations, while for four sources we have only a single epoch.

We fit the SEDs with the model of Granot & Sari (2002), developed for synchrotron emission from gamma-ray burst afterglows, and previously applied to the radio emission from TDEs (e.g., Zauderer et al. 2011; Cendes et al. 2021b, 2022b), using specifically the regime of $\nu_m \ll \nu_a$:

$$F_\nu = F_\nu(\nu_m)\left[\left(\frac{\nu}{\nu_m}\right)^2 e^{-s_4(\nu/\nu_m)^{2/3}} + \left(\frac{\nu}{\nu_m}\right)^{5/2}\right] \times \left[1 + \left(\frac{\nu}{\nu_a}\right)^{s_5(\beta_2-\beta_3)}\right]^{-1/s_5}, \quad (1)$$

---

[20] We note that in some other types of transients, such as supernovae (e.g., Chandra et al. 2009), shallow optically thick spectra have been observed and interpreted as inhomogeneities. In this case, the peak frequency and flux translate into limits on the radius of the outflow.

where $\beta_2 = 5/2$, $\beta_3 = (1 - p)/2$, $s_4 = 3.44p - 1.41$, and $s_5 = 1.47 - 0.21p$ (as in Eftekhari et al. 2018; Cendes et al. 2021a). Here, p is the electron energy distribution power-law index, $N(\gamma_e) \propto \gamma_e^{-p}$ for $\gamma_e \geqslant \gamma_m$, ν_m is the frequency corresponding to γ_m, ν_a is the synchrotron self-absorption frequency, and $F_\nu(\nu_m)$ is the flux normalization at $\nu = \nu_m$.

We determine the best-fit parameters of the model—$F_\nu(\nu_m)$, ν_a, and p—using the Python MCMC module `emcee` (Foreman-Mackey et al. 2013), assuming a Gaussian likelihood where the data have a log distribution for the parameters $F_\nu(\nu_m)$ and ν_a, and a lower limit of $\nu_a > 0.1$ GHz (where the upper range for $\nu_a = 2$–6 GHz, based on the existing frequency for the individual SED). For p we use a uniform prior of $p = 2$–4.0. We also include in the model a parameter that accounts for additional systematic uncertainty beyond the statistical uncertainty on the individual data points, $\sigma \lesssim 10\%$, which is a fractional error added to each data point. The posterior distributions are sampled using 100 MCMC chains, which were run for 3000 steps, discarding the first 2000 steps to ensure the samples have sufficiently converged by examining the sampler distribution.

Our population has a range of SED values, with a broad range in values in p ($p \approx 2$–3.6). Further, in some cases with multiple SEDs (ASASSN-14ae, AT2019ehz, and AT2019eve), we find the p value shows significant variation over several epochs. Such a range and variation have been seen in prior radio TDEs (e.g., Cendes et al. 2021b; Goodwin et al. 2022), and can be attributed to several causes. First, in the case of SEDs where ν_p is unconstrained, the paucity of data can lead to inconsistent values of p. Our remaining variation in p is within ranges in other TDEs (Berger et al. 2012; Cendes et al. 2021a; Goodwin et al. 2022). We thus adopt the values for p for specific TDEs as outlined in Section 4.1 for subsequent analysis.

Table 2
Spectral Energy Distribution Parameters

TDE	δt (days)	$F_{\nu,p}$ (mJy)	ν_p (GHz)	p
ASASSN-14ae[a]	2696	>0.329	<2.5	$2.25^{+0.24}_{-0.16}$
ASASSN-14ae[a]	3243	>0.720	<1.75	$2.05^{+0.10}_{-0.04}$
iPTF16fnl[a]	1752	>0.028	<5.0	$2.69^{+0.54}_{-0.48}$
PS16dtm[a]	1767	>0.361	<3.0	$2.14^{+0.25}_{-0.11}$
PS16dtm[a]	2291	>0.193	<1.75	$2.18^{+0.20}_{-0.12}$
AT2018dyb	1615	$0.50^{+0.06}_{-0.08}$	$1.41^{+0.33}_{-0.18}$	$2.96^{+0.24}_{-0.21}$
AT2018hco	1191	$0.26^{+0.02}_{-0.01}$	$4.37^{+0.38}_{-0.38}$	$3.03^{+0.32}_{-0.48}$
AT2018hco	1311	$0.25^{+0.06}_{-0.05}$	$2.75^{+0.56}_{-0.52}$	$2.84^{+0.13}_{-0.14}$
AT2018zr[a]	1743	>0.218	<1.75	$2.26^{+0.20}_{-0.17}$
AT2019dsg	796	$0.21^{+0.02}_{-0.02}$	$3.31^{+0.58}_{-0.58}$	$2.70^{+0.10}_{-0.11}$
AT2019ehz	970	$0.70^{+0.06}_{-0.06}$	$5.22^{+0.03}_{-0.03}$	$3.63^{+0.40}_{-0.34}$
AT2019ehz	1262	$0.23^{+0.03}_{-0.03}$	$2.96^{+0.05}_{-0.04}$	$2.55^{+0.45}_{-0.33}$
AT2019eve	945	$1.12^{+0.06}_{-0.06}$	$2.00^{+0.14}_{-0.14}$	$2.75^{+0.14}_{-0.17}$
AT2019eve	1102	$1.06^{+0.07}_{-0.07}$	$1.29^{+0.06}_{-0.06}$	$2.37^{+0.21}_{-0.17}$
AT2019eve	1325	$0.82^{+0.05}_{-0.06}$	$1.35^{+0.09}_{-0.06}$	$2.27^{+0.15}_{-0.14}$
AT2019teq[a]	1155	>0.492	<1.25	$2.97^{+0.38}_{-0.32}$

Note.

[a] Indicates SEDs in which the model peak is at or near the lowest-frequency data point, and the resulting values of $F_{\nu,p}$ and ν_p are lower and upper limits, respectively. We have combined data for some SEDs taken with different telescopes at roughly the same time for broader frequency coverage, and note these instances in Section 4.1.

4.1. Notes on Individual Tidal Disruption Events

The SED model fits are shown in Figures 4 and 5 and provide a good match to the data, although in the cases in Figure 5 we do not constrain ν_a. In these cases, we adopt the lowest-frequency data point as an upper limit, and the flux measured at that data point as a lower limit. The resulting model parameters are listed in Table 2. Below we summarize key results for the individual TDEs.

1. ASASSN-14ae has two SEDs obtained with the VLA at 2696 and 3243 days. In both cases, the SEDs peak below the lowest observed frequency. We thus use the lowest-frequency data point for each observation for the values of $F_{\nu,p}$ as a lower limit and ν_p as an upper limit. We use a mean value of $p = 2.15$ in the subsequent equipartition analysis.
2. PS16dtm has two SEDs obtained with the VLA at 1767 and 2291 days. In both cases the SEDs peak below the lowest observed data point, so we use the lowest data point for ν_p and $F_{\nu,p}$, and they are considered as upper and lower limits, respectively. We use a mean value of $p = 2.16$ in the subsequent equipartition analysis.
3. AT2018hco has two SEDs at 1191 days (VLA) and 1311 days (combined ATCA on 2022 April 22 and MeerKAT on 2022 May 7). We find that $F_{\nu,p}$ remained steady between the two observations, while ν_p decreased by about a factor of 1.6. We use a mean value of $p = 2.94$ in the subsequent equipartition analysis.
4. AT2019dsg had a single SED at 1171 days (VLA), and a partial SED at 1753 days (MeerKAT). While the latter does not allow for a full SED fit, it clearly indicates a brightening by a factor of ≈4 at low frequencies. At 1171 days, we find $p = 2.7$, consistent with the radio SEDs at earlier times (Cendes et al. 2021a). However, while $F_{\nu,p}$ exhibits a continued decline, ν_p increases to ≈3.5 GHz at 1171 days, while it was ≈1.7 GHz at 561 days (Cendes et al. 2021a); this increase creates the rise at 6 GHz seen in Figure 1.
5. AT2019ehz had two SEDs at 970 and 1262 days obtained with the VLA. We find that $F_{\nu,p}$ decreases by about a factor of 2 while ν_p decreases by about a factor of 1.5. We also find a decline in the value of p from about 3.6 to 2.6, and adopt a mean value of $p = 3.1$ in the subsequent equipartition analysis.
6. AT2019eve has three SEDs at 945 days (VLA), 1102 days (combined ATCA on 2022 April 30 and MeerKAT on 2022 May 10), and 1325 days (combined VLA on 2022 December 19 and MeerKAT on 2023 January 4). We note that $F_{\nu,p}$ remains steady at 945 and 1102 days, and then declines at 1325 days, while ν_p declines at 945 and 1102 days, but remains steady at 1325 days. We also find a decline in the value of p from about 2.75 to 2.3, and we use a mean value of $p = 2.46$ in the subsequent equipartition analysis.
7. iPTF16fnl has a single SED at 1752 days taken with the VLA. The SED is flat, with ν_p below our lowest data point, so we thus adopt values of $\nu_p < 5$ GHz and $F_{\nu,p} > 0.028$ mJy. We use $p = 2.69$ in the subsequent equipartition analysis.

8. AT2018dyb has a single SED at 1615 days (combined MeerKAT on 2022 December 11 and ATCA on 2023 January 22). We find $F_{\nu,p} \approx 0.25$ mJy, $\nu_p \approx 3$ GHz, and $p = 2.96$.
9. AT2018zr has a single SED at 1743 days obtained with the VLA. We find the SED peaks below our lowest observed frequency, and thus adopt $F_{\nu,p} > 0.329$ mJy, $\nu_p < 1.75$ GHz, and $p \approx 2.26$.
10. AT2019teq has a single SED at 1155 days obtained with the VLA. We find the SED peaks at the lowest observed frequency, indicating that the values of ν_p and $F_{\nu,p}$ may be considered as limits, and thus adopt $F_{\nu,p} > 0.492$ mJy, $\nu_p < 1.25$ GHz, and $p \approx 2.97$.

4.2. Equipartition Analysis

Using the inferred values of ν_p, $F_{\nu,p}$, and p (Table 2), we can now derive the physical properties of the outflows and ambient medium using an equipartition analysis. We assume the conservative case of a nonrelativistic spherical outflow; in Section 5.2 we demonstrate that none of the TDEs are in the regime where an off-axis relativistic jet interpretation can be supported (i.e., using the criterion in Matsumoto & Piran 2023). In the nonrelativistic spherical case the radius and kinetic energy are given by (see Equations (27) and (28) in Barniol Duran et al. 2013):

$$\begin{aligned} R_{\rm eq} \approx\ & (1 \times 10^{17}\ {\rm cm}) \times (21.8 \times 525^{p-1})^{\frac{1}{13+2p}} \chi_e^{\frac{2-p}{13+2p}} \\ & \times F_{p,\,{\rm mJy}}^{\frac{6+p}{13+2p}} d_{L,28}^{\frac{2(p+6)}{13+2p}} \nu_{p,10}^{-1} (1+z)^{\frac{-(19+3p)}{13+2p}} f_A^{\frac{-(5+p)}{13+2p}} f_V^{\frac{-1}{13+2p}} \\ & \times 4^{\frac{1}{13+2p}} \epsilon^{1/17} \xi^{\frac{1}{13+2p}}, \end{aligned} \tag{2}$$

$$\begin{aligned} E_{\rm eq} \approx\ & (1.3 \times 10^{48}\ {\rm erg}) \times [21.8^{\frac{-2(p+1)}{13+2p}}][525^{p-1} \\ & \times \chi_e^{2-p}]^{\frac{11}{13+2p}} F_{p,\,{\rm mJy}}^{\frac{14+3p}{13+2p}} d_{L,28}^{\frac{2(3p+14)}{13+2p}} \nu_{p,10}^{-1} (1+z)^{\frac{-(27+5p)}{13+2p}} \\ & \times f_A^{\frac{-(3(p+1)}{13+2p})} f_V^{\frac{2(p+1)}{13+2p}} 4^{\frac{11}{13+2p}} \xi^{\frac{11}{13+2p}} \\ & \times [(11/17)\epsilon^{-6/17} + (6/17)\epsilon^{11/17}], \end{aligned} \tag{3}$$

where d_L is the luminosity distance, z is the redshift, $f_A = 1$ and $f_V = \frac{4}{3} \times (1 - 0.9^3) = 0.36$ are the area and volume filling factors, respectively, where we assume that the emitting region is a shell of thickness 0.1 $R_{\rm eq}$, $\gamma_m = \max[\chi_e(\Gamma - 1), 2]$ is the minimum Lorentz factor as relevant for nonrelativistic sources, and $\chi_e = (p-2)/(p-1)\epsilon_e(m_p/m_e)$, where m_p and m_e are the proton and electron masses, respectively (Barniol Duran et al. 2013). The factors of $4^{\frac{1}{13+2p}}$ and $4^{\frac{11}{13+2p}}$ for the radius and energy, respectively, arise from corrections to the isotropic number of radiating electrons ($N_{e,\rm iso}$) in the nonrelativistic case. We further assume that the fraction of postshock energy in relativistic electrons is $\epsilon_e = 0.1$, which leads to correction factors of $\xi^{\frac{1}{13+2p}}$ and $\xi^{\frac{11}{13+2p}}$ in $R_{\rm eq}$ and $E_{\rm eq}$, respectively, with $\xi = 1 + \epsilon_e^{-1} \approx 11$. Finally, we parameterize any deviation from equipartition with a correction factor $\epsilon = (11/6)(\epsilon_B/\epsilon_e)$, where $\epsilon_B = 0.1$ is the fraction of postshock energy in magnetic fields.

Using $R_{\rm eq}$ we can also determine additional parameters of the outflow and environment (Barniol Duran et al. 2013): the magnetic field strength (B), the Lorentz factor of electrons radiating at ν_a (γ_a), and the number of radiating electrons (N_e):

$$\begin{aligned} B \approx\ & (1.3 \times 10^{-2}\ {\rm G}) \times F_{p,\,{\rm mJy}}^{-2} d_{L,28}^{-4} \\ & \times (1+z)^7 \nu_{p,10}^5 f_A^2 R_{{\rm eq},17}^4, \end{aligned} \tag{4}$$

$$\begin{aligned} \gamma_a \approx\ & 525 \times F_{p,\,{\rm mJy}} d_{L,28}^2 \nu_{p,10}^{-2} \\ & \times (1+z)^{-3} \frac{1}{f_A R_{{\rm eq},17}^2}, \end{aligned} \tag{5}$$

$$\begin{aligned} N_e \approx\ & (4 \times 10^{54}) \times F_{p,\,{\rm mJy}}^3 d_{L,28}^6 (1+z)^{-8} \\ & \times f_A^{-2} R_{{\rm eq},17}^{-4} \nu_{p,10}^{-5} \times (\gamma_a/\gamma_m)^{(p-1)}. \end{aligned} \tag{6}$$

We note an additional factor of 4 and a correction factor of $(\gamma_a/\gamma_m)^{p-1}$ are added to N_e for the nonrelativistic regime (Barniol Duran 2024, private communication). We determine the ambient density assuming a strong shock and an ideal monatomic gas as $n_{\rm ext} = N_e/4V$, where the factor of 4 is due to the shock jump conditions and V is the volume of the emitting region as defined above.

Finally, the synchrotron cooling frequency, ν_c, is given by (Sari et al. 1998):

$$\nu_c \approx 2.25 \times 10^{14} B^{-3} \Gamma^{-1} t_d^{-2}\ {\rm Hz}, \tag{7}$$

where t_d refers to the age of the system, and here $\Gamma \approx 1$. The inferred values for ν_c are listed in Table 3. In several cases (e.g., AT2018hco and AT2019ehz) the value of ν_c is within the frequency range of our data, but we do not observe a cooling break. This may be indicative of an incorrect value for t_d in Equation (7) due to a delayed outflow, as we discuss in Section 4.3. Another possibility is that the value of ϵ_B is lower than our fiducial assumption of 0.1, and hence the outflow may not be in equipartition. Although such deviations have been measured in TDEs in the past (Eftekhari et al. 2018; Cendes et al. 2021a), given the lack of evidence for such a deviation in our data we choose to conservatively assume no deviation is present. We note that our energy values are thus a lower limit and would be higher if a deviation from equipartition is assumed.

The inferred equipartition values for the nine new TDEs with SEDs reported in this paper, and for the TDE with a distinct late-time component (AT2019dsg), and iPTF16fnl, are listed in Table 3. Using the inferred values of $R_{\rm eq}$ we calculate the mean expansion velocity at each epoch, $\beta = v/c$, assuming that the outflow was launched at the time of optical discovery.

4.3. Estimated Outflow Launch Timescales

Using the time of optical discovery as an initial estimate for the outflow launch date, the inferred velocities are in the range $\beta \approx 0.008$–0.07 (Table 3), with the lowest velocities inferred for the older TDEs in our sample. However, for TDEs that have more than one SED where we directly measure the peak (AT2019eve, AT2019ehz, and AT2018hco), we find higher values for β by comparing the radius measurements between SED epochs than what we infer from individual epochs with the assumption that the outflow began at the time of optical discovery. This indicates that the assumption of a launch date that roughly coincides with the optical discovery is incorrect, as also indicated by the nondetections at earlier times.

Table 3
Equipartition Model Parameters

Object	δt (days)	$\log(R_{\rm eq})$ (cm)	$\log(E_{\rm eq})$ (erg)	$\log(B)$ (G)	$\log(N_e)$	$\log(n_{\rm ext})$ (cm^{-3})	β	$\log(\nu_c)$ (Hz)
ASASSN-14ae[a]	2696	>16.61	>47.70	<-0.54	>53.02	<2.54	>0.006	>9.10
ASASSN-14ae[a]	3423	>16.92	>48.26	<-0.72	>53.59	<2.16	>0.010	>9.15
iPTF16fnl[a]	1752	>15.37	>44.79	<-0.13	>50.55	<3.79	>0.0005	>8.24
PS16dtm[a]	1767	>16.77	>48.10	<-0.58	>52.68	<1.72	>0.014	>9.59
PS16dtm	2291	>16.86	>47.99	<-0.77	>52.57	<1.32	>0.013	>9.96
AT2018dyb	1615	$16.53^{+0.05}_{-0.03}$	$46.90^{+0.52}_{-0.29}$	$-0.83^{+0.23}_{-0.12}$	$52.54^{+0.08}_{-0.12}$	$2.23^{+0.13}_{-0.20}$	$0.008^{+0.002}_{-0.002}$	$10.42^{+0.15}_{-0.11}$
AT2018hco	1191	$16.55^{+0.10}_{-0.07}$	$47.76^{+1.06}_{-0.63}$	$-0.43^{+0.39}_{-0.24}$	$53.10^{+0.14}_{-0.13}$	$2.78^{+0.31}_{-0.15}$	$0.012^{+0.003}_{-0.002}$	$9.48^{+1.24}_{-1.42}$
AT2018hco	1311	$16.60^{+0.17}_{-0.12}$	$47.58^{+1.21}_{-0.90}$	$-0.59^{+0.39}_{-0.30}$	$52.91^{+0.21}_{-0.13}$	$2.44^{+0.39}_{-0.42}$	$0.012^{+0.01}_{-0.01}$	$9.88^{+1.14}_{-1.40}$
AT2018zr[a]	1743	>16.84	>47.91	<-0.78	>52.51	<1.34	>0.016	>10.21
AT2019dsg	1171	$16.44^{+0.08}_{-0.07}$	$47.29^{+0.32}_{-0.30}$	$-0.50^{+0.13}_{-0.12}$	$52.80^{+0.10}_{-0.09}$	$2.82^{+0.17}_{-0.17}$	$0.009^{+0.002}_{-0.002}$	$9.71^{+0.03}_{-0.04}$
AT2019ehz	970	$16.61^{+0.03}_{-0.03}$	$47.95^{+0.04}_{-0.04}$	$-0.41^{+0.02}_{-0.02}$	$53.37^{+0.05}_{-0.05}$	$2.87^{+0.05}_{-0.06}$	$0.017\ ^{+0.001}_{-0.001}$	$9.62^{+0.06}_{-0.06}$
AT2019ehz	1262	$16.63^{+0.05}_{-0.05}$	$47.68^{+0.07}_{-0.07}$	$-0.59^{+0.05}_{-0.05}$	$53.04^{+0.09}_{-0.07}$	$2.48^{+0.08}_{-0.11}$	$0.014\ ^{+0.002}_{-0.002}$	$9.91^{+0.13}_{-0.16}$
AT2019eve	945	$17.18^{+0.03}_{-0.03}$	$48.86^{+0.04}_{-0.04}$	$-0.81^{+0.03}_{-0.03}$	$54.38^{+0.25}_{-0.24}$	$2.19^{+0.28}_{-0.26}$	$0.061^{+0.003}_{-0.004}$	$10.83^{+0.08}_{-0.10}$
AT2019eve	1102	$17.34^{+0.02}_{-0.02}$	$49.00^{+0.04}_{-0.04}$	$-0.99^{+0.03}_{-0.03}$	$54.02^{+0.29}_{-0.32}$	$1.35^{+0.30}_{-0.31}$	$0.075^{+0.004}_{-0.004}$	$11.24^{+0.08}_{-0.08}$
AT2019eve	1325	$17.28^{+0.03}_{-0.03}$	$48.84^{+0.05}_{-0.05}$	$-0.98^{+0.03}_{-0.03}$	$53.66^{+0.23}_{-0.25}$	$1.16^{+0.22}_{-0.24}$	$0.056^{+0.004}_{-0.004}$	$11.04^{+0.08}_{-0.08}$
AT2019teq[a]	1155	>17.23	>48.65	<-0.99	>53.31	<0.97	>0.06	>11.21

Notes. The values in this table are calculated using an outflow launch time based on the optical discovery date, with errors propagated from the ν_p and $F_{\nu,p}$ errors in Table 2.

[a] Indicates an unconstrained SED, where the resulting values can be considered as limits.

Thus, we estimate the launch dates of the outflows following the method in Cendes et al. (2022b); namely, we fit the radius evolution with a linear trend and determine the timescale at which $R = 0$. This analysis requires multiple SEDs, and so we only carry it out for five TDEs (ASASSN-14ae, PS16dtm, AT2018hco, AT2019ehz, and AT2019eve). Since all of these TDEs also have an initial single-frequency (6 GHz) detection before an SED was obtained, we extract a rough radius estimate from this first detection by estimating the value of ν_p at that time from its later evolution, and calibrating $F_{\nu,p}$ to match the observed 6 GHz flux density. In the case of AT2019eve, the third (latest) SED exhibits a decrease in $F_{\nu,p}$ while ν_p remains relatively steady, resulting in a decrease in the inferred radius compared to ≈200 days earlier. As the first two measured radii for AT2019eve show an increase, and the third SED occurred during a continued decrease of the light curve, we conclude it is more likely to be related to a change in the outflow's structure related to deceleration, which would not be useful for estimating the launch time of the outflow, and thus do not include this last data point in our calculation. For ASASSN-14ae and PS16dtm, where the peak of emission appears to be below our lowest data point, we extract a rough radius estimate based off the lowest data point directly measured ($\nu_p = 1.75$ GHz in both cases), and assume ν_p is fixed at this value throughout our observation.

In Figure 6, we show our fits to the radius data for each TDE (including for reference the date of the last measured upper limit). In all cases, with the exception of AT2019ehz and PS16dtm, we find significant delays in the outflow launch time, of ≈545–2150 days; see Table 4. Equally important, the inferred time delays are consistent with with the available radio nondetections. In the case of AT2019ehz, the data do not converge to a launch time because the decreases in peak flux and peak radius correspond with a very small increase in radius. It is possible, given that it was brightest when first detected, that the outflow had already decelerated, which is why the radius is not zero at the launch date in our analysis. Deceleration of the outflow could also potentially explain the lack of convergence in our data for PS16dtm. For ASASSN-14ae, we note since our radii used in this calculation are upper limits, the inferred launch date is also a limit, and could be even earlier.

In the case of TDEs with only a single SED, and for AT2019ehz and PS16dtm where our multiepoch radius analysis did not converge, we instead make individual estimates of the launch date using the observed light-curve behavior and prior upper limits. For AT2019dsg, which exhibits a distinct late-time component, we use an outflow launch time of 561 days, corresponding to the dimmest light-curve point before the rebrightening. For AT2018zr, with a constraining upper limit at 1218 days, we assume the outflow launched at that time. For PS16dtm, we adopt the last constraining upper limit in radio observations at 984 days. For AT2019teq, with a constraining upper limit at 351 days, we assume the outflow launched at that time. For AT2018dyb, which has brightened by an order of magnitude between our two observations, we assume the outflow launch time corresponds to our initial detection at 1028 days. Finally, for AT2019ehz, which has a data gap of ≈730 days between the final upper limit and the first detection, we assume that the light curve rose at roughly the same rate as its observed decline, giving an estimated launch time of ∼400 days. We note that while we are currently limited for these TDEs by the cadence of observations, planned future observations of the TDEs with only a single SED will allow us to better refine the outflow launch times, and potentially increase our precision with estimates for the TDEs in Figure 6.

With the outflow delay estimates we recalculate the values of β and ν_c, which are strongly dependent on the chosen launch time (Table 4). We find that this increases the inferred velocities by a factor of ≈2–5, to $\beta \approx 0.02$–0.15.

Finally, we note that for all but one TDE, the revised ν_c is more in line with the data, and include these values here as a consistency check. Specifically, in most cases if we calculate ν_c from the time of optical discovery (Table 3), we would expect a cooling break to be present in the range of frequencies covered

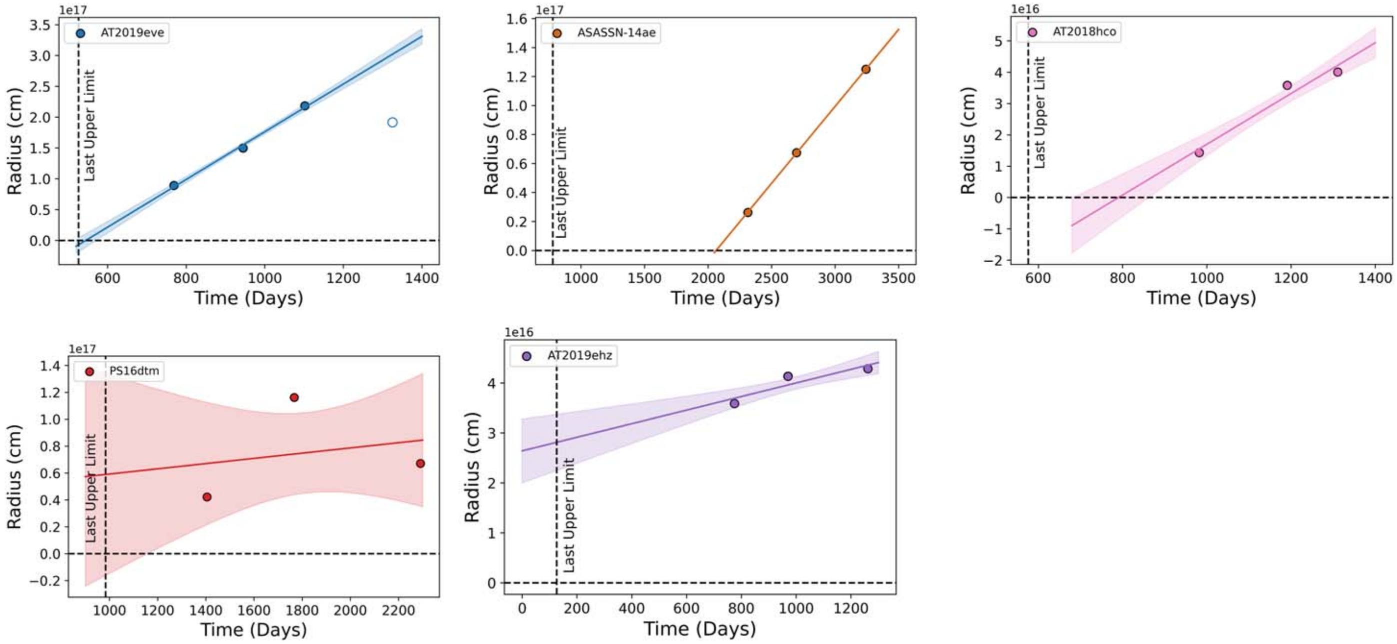

Figure 6. Equipartition radius as a function of time for each TDE with multiple SEDs. The lines are linear fits to the radius evolution to determine the outflow launch time. For reference we include the date of the last upper limit (vertical dashed lines). The first data point for each TDE is inferred from a 6 GHz detection and the subsequent evolution of the SEDs (see Section 4.3). For AT2019eve, we exclude the last SED point and show it as an open circle.

Table 4
Parameters with Delayed Outflows

TDE	Outflow Start (days)	$\delta t_{\rm ori}$ (days)	$\delta t_{\rm rev}$ (days)	β	$\log(\nu_c)$ (Hz)
TDEs with Launch Times Estimated from the Radius Evolution					
ASASSN-14ae	$<2064^{+3}_{-6}$	2696	632	>0.025	>10.36
ASASSN-14ae	$<2064^{+3}_{-6}$	3243	1179	>0.028	>10.39
AT2018hco	790^{+70}_{-110}	1191	401	$0.039^{+0.016}_{-0.015}$	$10.42^{+0.04}_{-0.04}$
AT2018hco	790^{+70}_{-110}	1311	521	$0.043^{+0.010}_{-0.011}$	$10.79^{+0.03}_{-0.03}$
AT2019eve	545^{+30}_{-30}	945	400	$0.139^{+0.012}_{-0.014}$	$11.55^{+0.11}_{-0.13}$
AT2019eve	545^{+30}_{-30}	1102	557	$0.153^{+0.014}_{-0.013}$	$11.82^{+0.11}_{-0.11}$
AT2019eve	545^{+30}_{-30}	1325	780	$0.094^{+0.016}_{-0.016}$	$11.43^{+0.11}_{-0.11}$
TDEs with Individually Inferred Launch Times					
PS16dtm	984	1767	783	>0.030	>10.30
PS16dtm	984	2291	1307	>0.023	>10.45
AT2018zr	1218	1743	525	>0.043	>11.09
AT2019dsg	561	1171	610	$0.017^{+0.002}_{-0.002}$	$10.25^{+0.03}_{-0.04}$
AT2018dyb	1028	1615	270	$0.023^{+0.002}_{-0.002}$	$11.32^{+0.11}_{-0.11}$
AT2019ehz	400	945	545	$0.029^{+0.001}_{-0.001}$	$10.01^{+0.11}_{-0.11}$
AT2019ehz	400	1262	862	$0.020^{+0.002}_{-0.002}$	$10.23^{+0.11}_{-0.11}$
AT2019teq	351	1155	804	>0.080	>11.51

Note. The outflow start times are in days post–optical discovery, where $\delta t_{\rm ori}$ are the original outflow dates using the date since optical detection, and $\delta t_{\rm rev}$ are the revised times of our SED observations relative to the outflow start times.

by our SEDs. However, no such break is discernible, implying the cooling break is higher than calculated. The exception to this is AT2019ehz, for which an estimated launch date was not possible via a fit to its radius evolution. This discrepancy in ν_c resolves itself once we use a shorter δt in its calculation, which, however, implies a delayed outflow. However, other explanations are also possible due to the parameters required to calculate ν_c, such as a deviation from equipartition. We note that even if a deviation from equipartition is present, it minimally affects the radius (see Equation (2)), and thus would not significantly change our estimated outflow times.

5. Discussion

5.1. Outflow and Environment Properties of Tidal Disruption Events with Late Radio Emission

Our equipartition analysis for eight TDEs with delayed radio emission and two TDEs with a second flare allows us to examine their energy and velocity relation, and to compare their properties to TDEs with early radio emission. In Figure 7 we plot the kinetic energy (E_K) and velocity ($\Gamma\beta$) for all known optical TDEs with radio detections for which a similar analysis has been carried out, using the highest energy inferred in those sources from Table 3 and the literature (Zauderer et al. 2011; Alexander et al. 2016; Cendes et al. 2021a, 2021b, 2022b; Stein et al. 2021; Goodwin et al. 2022, 2023c). We also include the jetted, nonoptical TDE Sw J1644+57 for reference (Eftekhari et al. 2018; Cendes et al. 2021b). For TDEs where we obtained lower limits for these values, we include an arrow in the direction of the allowable phase space. For TDEs with late emission, with the exception of iPTF16fnl (which had a lower limit at $E_K > 10^{45}$ erg and $\Gamma\beta > 0.002$), we find they span $E_K \approx 10^{47}$–10^{49} erg, and $\Gamma\beta \approx 0.01$–0.1. Overall, we find the majority of the TDE population in our sample show velocity and energy values similar to that seen in a broader population of TDEs with nonrelativistic outflows that have emission at early times ($\sim 10^{47}$–10^{49}; i.e., Alexander et al. 2016; Cendes et al. 2021a).

In Figure 8 we show the inferred ambient density for each TDE as a function of radius (scaled by the Schwarzschild radius) for the TDEs in our sample and previously studied radio-emitting TDEs. Here we use the mass for each black hole inferred from optical data (Blagorodnova et al. 2017;

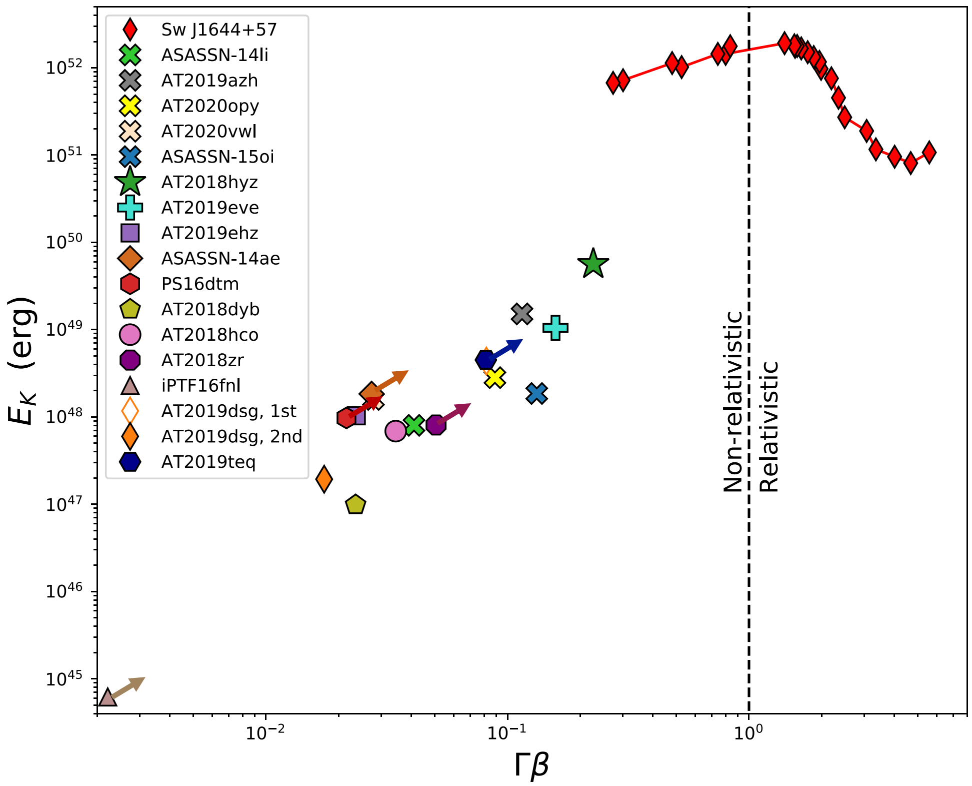

Figure 7. Kinetic energy versus velocity for the new TDEs presented in this work (and AT2018hyz; Cendes et al. 2022b). We use the inferred launch times in Table 4, and where our observations resulted in an upper limit we include an arrow in the direction of allowable energy/velocity phase space. For comparison we include optically discovered TDEs with early radio emission (sideways triangles; Alexander et al. 2016; Cendes et al. 2021a; Stein et al. 2021; Goodwin et al. 2022, 2023b, 2023c) and Sw J1644+57 (red diamonds; Zauderer et al. 2011; Cendes et al. 2021b). In the cases of AT2019azh and AT2020opy (Goodwin et al. 2022, 2023c), we show the peak energy and velocity adjusted to $\epsilon_B = 0.1$. For ASASSN-15oi (Horesh et al. 2021a), we use the observation with the highest peak frequency and peak luminosity (182 days) with $\epsilon_B = 0.1$ and $p = 2.39$, which best fit the observed SED, and infer the velocity by subtracting 90 days (the last date of nondetection; see Horesh et al. 2021a). We also include the peak energy and velocity in the first peak for AT2019dsg for reference (open orange diamond; Cendes et al. 2021a; Stein et al. 2021).

Leloudas et al. 2019; Nicholl et al. 2019; Goodwin et al. 2022, 2023c; Hammerstein et al. 2023; Yao et al. 2023). In the cases of TDEs where we have upper limits on density and lower limit on radius, we include an arrow in the direction of the allowable phase space. We find that the densities probed are consistent with the densities and circumnuclear (CNM) density profiles of previous TDEs, and are more dense than the low-density environment of M87*. Crucially, we do not infer an unusually high density for any TDEs in our sample, which might be expected if the radio emission was delayed due to rapid shift from low to high density.

As many of our light curves are still rising, this implies that the blast wave is still in the free expansion phase (with $v \approx$ constant). In this case, the mass of the swept-up material, $M_{\rm swept}$, would be less than the mass of the ejecta, $M_{\rm ej}$. Using the inferred ambient densities, kinetic energies, and velocities inferred from the equipartition analysis we verify that $M_{\rm swept} \lesssim M_{\rm ej}$ for all TDEs except for AT2019eve, where $M_{\rm swept} \gtrsim M_{\rm ej}$ in the first observation at 945 days and $M_{\rm swept} \approx M_{\rm ej}$ in our second observation at 1102 days. Given the steady fading light curve of AT2019eve during this time period, we conclude AT2019eve is no longer in free expansion.

We can consider the case of the X-ray TDE IGRJ12580+0134, which had a radio-only flare observed ~1600 days after peak (Perlman et al. 2022). Perlman et al. (2022) interpret this flare is most likely due to a jet outflow encountering a CNM cloud at $\approx 2.9-3 \times 10^{18}$ cm from an $\sim 10^5 \, M_\odot$ black hole (Irwin et al. 2015), where the density increases from a background of 5.2 cm^{-3} to 10.3 cm^{-3}. These densities would be lower than what we sample in our TDE population and at larger radii than we probe in our work ($R/R_s > 10^7$), and the outflow velocity of $v \approx 0.17$ is higher than what we infer for all our TDEs. However, as Perlman et al. (2022) note theirs is a simplified model with several degeneracies, and other values may fit the data.

5.2. *Off-axis Jets*

We explore the possibility that the late radio emission is due to relativistic jets with an off-axis viewing orientation. First, we note that if the origin of the delayed radio emission was an off-axis relativistic jet, then the inevitable conclusion based on our detection statistics (Section 3.2) is that about half of all optically selected TDEs harbor off-axis jets. This conclusion, which would indicate a rate of order a few hundred per cubic gigaparsec per year (using the optical TDE rate from van Velzen 2018), is in strong conflict with the rate of on-axis relativistic jets determined from gamma rays and optical detections (Brown et al. 2015; Andreoni et al. 2022) of $\sim$0.01–0.02 Gpc^{-3} yr^{-1} and a beaming correction factor of $\sim 10^2$.

Further, we can consider two possible off-axis jet scenarios: (i) an initially off-axis relativistic jet that has decelerated to a nonrelativistic velocity and spread to roughly spherical

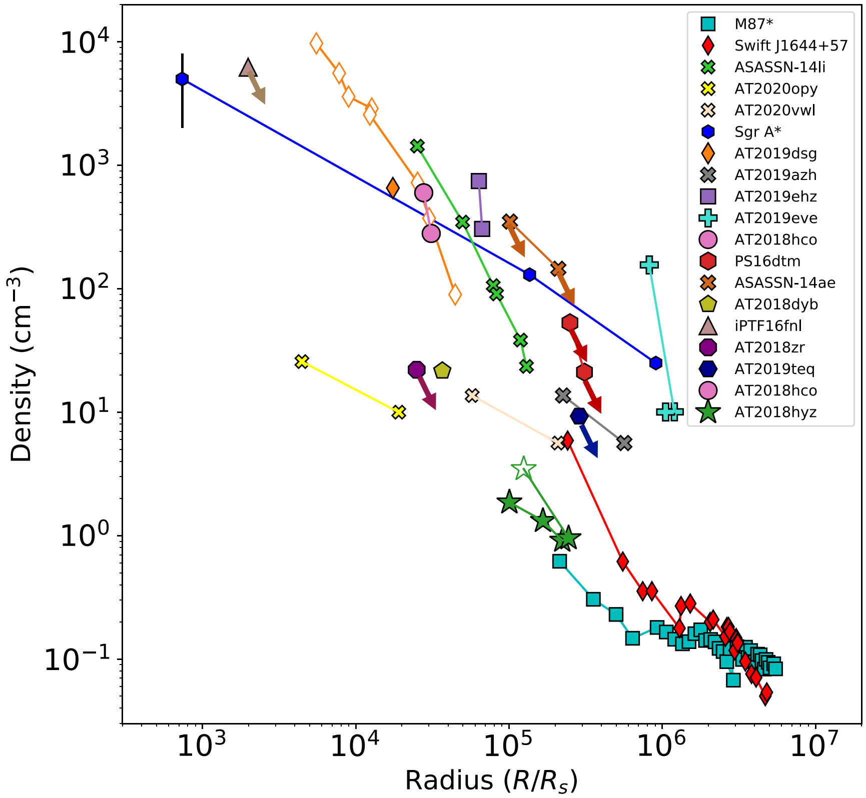

Figure 8. The CNM density profiles inferred for the TDEs presented in this work (and AT2018hyz; Cendes et al. 2021a), normalized to the Schwarzschild radius of each SMBH. We also include for comparison the density profiles for the optically discovered TDEs with early radio emission (sideway triangles; Alexander et al. 2016; Cendes et al. 2021a; Horesh et al. 2021a; Goodwin et al. 2022, 2023b, 2023c), Sw J1644+57 (Berger et al. 2012; Zauderer et al. 2013; Eftekhari et al. 2018; Cendes et al. 2021b), the Milky Way (Baganoff et al. 2003; Gillessen et al. 2019), and M87 (Russell et al. 2015). For TDEs where our density value is an upper limit, we include an arrow in the direction of the phase space of the allowable values.

geometry, which is mainly relevant for the TDEs in our sample in which we have observed the light curves peak and decline; and (ii) an off-axis jet that remains collimated and oriented off axis, which is potentially relevant for TDEs in which the radio emission is still rising (e.g., Matsumoto & Piran 2023).

In the first scenario, the time at which the radio emission peaks is given by the deceleration time (e.g., Nakar & Piran 2011):

$$t_{\rm dec} \approx 30 \text{ days } E_{{\rm eq},49}^{1/3} n_{\rm ext}^{-1/3} \beta_0^{-5/3}, \qquad (8)$$

where β_0 is the initial velocity, which for an off-axis relativistic jet is $\beta_0 = 1$. Using the results of our equipartition analysis (Section 4.2), we find $t_{\rm dec} \lesssim 100$ days for all TDEs in our sample, which is substantially smaller than the observed peak timescales of $\gtrsim$700 days. This agrees with the much lower luminosities compared to Sw J1644+57, which became nonrelativistic at a comparable timescale of ≈700 days (Eftekhari et al. 2018). In particular, several of the TDEs in our sample (i.e., PS16dtm, AT2018hco, AT2019ehz, and AT2019eve) peaked at ∼700–1700 days with luminosities of $\sim 10^{38}$–10^{39} erg s^{-1}, about 2 to 3 orders of magnitude below Sw J1644+57. These TDEs consistently have values of $\beta \approx 0.01$–0.07 and have already peaked, so following the formalism of Matsumoto & Piran (2023) and Beniamini et al. (2023) we conclude that they cannot be off-axis jets since they do not cross the threshold of $\beta \approx 0.44$ required for a decelerating off-axis jet.

The second scenario involves the possibility of a decelerating off-axis jet that remains collimated with the emitting area increasing over time, as suggested for the delayed rapid rise in AT2018hyz by Matsumoto & Piran (2023) and Sfaradi et al. (2024). In updated work, Beniamini et al. (2023) propose a threshold of $\beta \approx 0.44$ below which two solutions exist: a nonrelativistic spherical outflow and an off-axis relativistic jet. Critically, in the latter scenario, as the jet decelerates and the emission area grows, the outflow will eventually exceed the threshold value. For the TDEs in our sample with rising light curves (i.e., ASASSN-14ae, AT2018dyb, and AT2018zr) we find values for $\beta \approx 0.01 \ll 0.44$. Since these sources still exhibit rising emission, continued monitoring will establish whether they ever cross the threshold value of β. However, this is unlikely given their current evolution. For example, in the case of ASASSN-14ae, which is rising rapidly after a long delay of $\gtrsim$2300 days, we find that with its current evolution ($F_{\nu,p} \propto t^{4.4}$, $\nu_p \approx$ const) it is expected to follow $\beta \propto t^{1.1}$, and hence will cross the threshold of 0.23 (0.44) in ≈17 (≈31) yr given the current value of $\beta \approx 0.01$; at that point it will reach a peak luminosity of a few times 10^{43} erg s^{-1}, much in excess of the peak luminosity of Sw J1644+57. Similar conclusions are reached for AT2018dyb and AT2018zr, which begin rising at $\approx 10^3$ days.

We next note the case of AT2019dsg, which exhibits early radio emission (i.e., peaking at ∼200–400 days) and then rapidly rises again a second time. We could envision a scenario in which this TDE produced both a spherical nonrelativistic outflow that dominates the early radio emission, and an off-axis relativistic jet. The inferred velocities for this TDE are low, $\beta \approx 0.003$–0.009, and hence they are again unlikely to eventually cross the threshold of $\beta \approx 0.44$ expected for an off-axis jet. As for the other TDEs with rising light curves, continued monitoring of AT2019dsg will elucidate the origin of its emission.

Thus, we conclude based on the measured radio properties (timescales and luminosities), the inferred physical properties (velocities), and the rate of TDEs with late radio emission that off-axis jets are an unlikely explanation for this population.

5.3. *Origin of the Delayed Outflows*

There are at least two broad possibilities for the origin of the delayed mildly relativistic outflow, both of which connect to its assumed origin in a fast outflow from the innermost regions of the black hole accretion flow. We note explicitly that it is possible that late-time radio emission is of diverse origins, given the range of behavior in terms of parameters such as the timescales, luminosities, rise rates, and other features. Additional observations of radio TDEs at late times will allow us to distinguish between scenarios.

One possibility is that the delayed radio emission is due to the timescales for debris circularization and viscous accretion (Hayasaki & Jonker 2021). In this scenario, the first stream–stream collisions produce the optical/UV flare, creating a circularized debris ring. The ring then evolves viscous diffusively, and reaches the innermost stable circular orbit (ISCO) on a timescale of months to years after the initial flare, consistent with the timescale we infer for our TDEs. However, with a disk wind velocity of $\sim 0.4c$, this is inconsistent with the velocities we infer for our TDEs, although may be possible to achieve if the outflow mass was very low or the radius for the ISCO was exceptionally large.

Alternately, it is also possible that the formation of a jet or fast wind from the inner accretion flow is delayed because the SMBH accretion rate does not peak on the same timescale as the mass fallback rate. Because the debris from the TDE is weakly bound to the SMBH, its natural configuration is a large quasi-spherical envelope (e.g., Loeb & Ulmer 1997; Coughlin & Begelman 2014), which must cool and radially contract to form an accretion disk (e.g., Metzger 2022). If accretion onto the SMBH supplies energy to the envelope (with an efficiency η), full contraction of the envelope can be delayed for a time, up to $\sim$700 days (e.g., Loeb & Ulmer 1997), in agreement with the timescales of the outflows measured in this work. Thus, we see that disk formation can be delayed for hundreds to thousands of days, providing an alternative explanation for late-onset radio-generating outflows from the SMBH (Metzger 2022). This model also appears to provide a good description of the multiwavelength properties of ASASSN-15oi (A. Hajela et al. 2024, in preparation). As another alternative possibility, the escape of a jet from the vicinity of the black hole may be delayed until processes within the accretion flow align the angular momentum axis of the accretion disk and the jet to the black hole spin axis (Teboul & Metzger 2023).

We note explicitly that it is possible that late-time radio emission is of diverse origins, given the range of behavior in terms of parameters such as the timescales, luminosities, rise rates, and other features. Additional observations of radio TDEs at late times will allow us to distinguish between scenarios.

6. Conclusions

We presented radio observations for 23 optically discovered TDEs on timescales of ≈500–3200 days postdiscovery. We detected radio emission from 17 of these TDEs, of which six had an ambiguous or host/AGN origin. Of the 11 TDEs with transient radio emission, nine TDEs were detected for the first time despite a lack of radio emission at earlier times, and one TDE (AT2019dsg) was detected to significantly brighten at late time relative to its declining radio emission at earlier times; this late-time component is similar to what has been found in ASASSN-15oi and AT2020vwl (Horesh et al. 2021a; Goodwin et al. 2023a, 2023b). Based on this large sample, our key results are as follows.

1. We find ≈40% of TDEs in this work show late-time emission, meaning a substantial fraction of all optically selected TDEs exhibit radio emission that rises on timescales of hundreds of days.
2. The range of luminosities for this sample is $\sim 10^{37}$–10^{39} erg s^{-1}, though in some cases this is a lower limit because the emission is still rising.
3. We find radio emission in this population peaks at timescales 700–3200 days, though we note some are lower limits as the emission is still rising.
4. Multifrequency SEDs reveal a range of peak frequencies of $\lesssim 1$ GHz to ≈5 GHz. Using the SED information we determine the outflow physical properties assuming equipartition. We find $R_{\rm eq} \approx 3 \times 10^{16}$–$2 \times 10^{17}$ cm and $E_K \approx 8 \times 10^{46}$–$1 \times 10^{49}$ erg.
5. Using the radius evolution when available, and the light-curve behavior otherwise, we infer outflow launch timescales of ≈500–2000 days. This then leads to inferred velocities of $\beta \approx 0.02$–0.15.
6. From the equipartition analysis we also infer CNM densities of $\approx 10^{1}$–10^{4} cm^{-3}. These densities are comparable to those inferred for TDEs with early radio emission.
7. We rule out off-axis relativistic jets as an explanation for the bulk of the TDEs with late radio emission, and conclude delayed outflows are a more likely explanation. If this delay is due to delayed disk formation, then the relative formation timescale inferred from our data is $\sim$700 days.

Our study highlights that persistent radio monitoring of TDEs starting after discovery and lasting for several years is critical for determining the timing of outflow formation, and its subsequent evolution; this includes TDEs that exhibit radio emission at early time, but which may rebrighten subsequently. Additionally, multifrequency observations, extending below $\sim$1 GHz, are crucial for determining the outflow properties (energy and velocity) and the ambient density. As demonstrated here, these observations are within reach for TDEs at modest distances with existing facilities (VLA, ATCA, and MeerKAT). In the future, much larger samples of TDEs (typically at larger distances) from the Vera C. Rubin Observatory Legacy Survey of Space and Time will be effectively studied with the next-generation Square Kilometer Array and the next-generation VLA.

Acknowledgments

We thank Tatsuya Matsumoto and Nick Stone for their helpful discussions on TDEs. The Berger Time-Domain Group at Harvard is supported by NSF and NASA grants. The National Radio Astronomy Observatory is a facility of the National Science Foundation operated under cooperative agreement by Associated Universities, Inc. The MeerKAT telescope is operated by the South African Radio Astronomy Observatory, which is a facility of the National Research Foundation, an agency of the Department of Science and Innovation. The Australia Telescope Compact Array is part of the Australia Telescope National Facility (https://ror.org/05qajvd42), which is funded by the Australian Government for operation as a National Facility managed by CSIRO. This research has made use of the CIRADA cutout service at cutouts.cirada.ca, operated by the Canadian Initiative for Radio Astronomy Data Analysis (CIRADA). CIRADA is funded by a grant from the Canada Foundation for Innovation 2017 Innovation Fund (Project 35999), as well as by the Provinces of Ontario, British Columbia, Alberta, Manitoba, and Quebec, in collaboration with the National Research Council of Canada, the US National Radio Astronomy Observatory, and Australia's Commonwealth Scientific and Industrial Research Organisation.

Appendix

The properties of all 24 TDEs in our sample are provided in Table 5. Data for excluded objects are included for completeness in Table 6.

Table 5
Radio Observations of Tidal Disruption Events

Object	Telescope	Project Code/ Source	Date of Observation	δt (days)	Frequency (GHz)	Flux Density (mJy)
iPTF16fnl	VLA	20A-492	2020 May 24	1365	6	0.045 ± 0.001
	⋯	21A-303	2021 Jun 15	1752	3	<0.514
	⋯	⋯	⋯	⋯	5	0.028 ± 0.008
	⋯	⋯	⋯	⋯	7	0.031 ± 0.007
	⋯	⋯	⋯	⋯	9	0.024 ± 0.006
	⋯	⋯	⋯	⋯	11	0.023 ± 0.008
AT2019dsg	VLA	21A-303	2021 Jun 12	796	1.25	<0.514
	⋯	⋯	⋯	⋯	1.75	0.114 ± 0.033
	⋯	⋯	⋯	⋯	2.5	0.235 ± 0.026
	⋯	⋯	⋯	⋯	3.5	0.201 ± 0.014
	⋯	⋯	⋯	⋯	5	0.209 ± 0.014
	⋯	⋯	⋯	⋯	7	0.132 ± 0.013
	MeerKAT	SCI-20220822-YC-01	2023 Jan 15	1378	0.88	0.284 ± 0.041
	⋯	⋯	⋯	⋯	1.36	0.384 ± 0.026
	VLA	VLASS 3	2023 Jan 31	1404	3	<0.386
	MeerKAT	SCI-20220822-MB-03	2023 Mar 5	1437	1.36	0.228 ± 0.016
ASASSN-14ae	VLA	15B-247	2016 Mar 12	778	5	<0.033
	⋯	VLASS 1	2019 Nov 19	2122	3	<0.420
	⋯	20A-492	2020 May 25	2313	6	0.090 ± 0.015
	⋯	21A-303	2021 Jun 12	2696	3	0.334 ± 0.038
	⋯	⋯	⋯	⋯	5	0.222 ± 0.018
	⋯	⋯	⋯	⋯	7	0.169 ± 0.007
	⋯	⋯	⋯	⋯	9	0.155 ± 0.010
	⋯	⋯	⋯	⋯	11	0.150 ± 0.001
	⋯	VLASS 2	2021 Dec 4	2608	3	<0.47
	⋯	22B-205	2022 Dec 11	3243	1.25	<3.12
	⋯	⋯	⋯	⋯	1.75	0.720 ± 0.041
	⋯	⋯	⋯	⋯	2.5	0.680 ± 0.029
	⋯	⋯	⋯	⋯	3.5	0.604 ± 0.017
	⋯	⋯	⋯	⋯	5	0.418 ± 0.080
	⋯	⋯	⋯	⋯	7	0.446 ± 0.011
	⋯	⋯	⋯	⋯	9	0.382 ± 0.020
	⋯	⋯	⋯	⋯	11	0.361 ± 0.025
	⋯	⋯	⋯	⋯	13.5	0.347 ± 0.015
	⋯	⋯	⋯	⋯	16.5	0.337 ± 0.022
	⋯	⋯	⋯	⋯	20	0.303 ± 0.015
	⋯	⋯	⋯	⋯	24	0.343 ± 0.014
PS16dtm	VLA	16B-398	2016 Sept 22	54	15.5	<0.069
	⋯	⋯	2016 Dec 21	144	6	<0.075
	⋯	⋯	2017 Jun 4	326	3	<0.0323
	⋯	⋯	2017 Aug 22	372	6	<0.075

Table 5
(Continued)

Object	Telescope	Project Code/ Source	Date of Observation	δt (days)	Frequency (GHz)	Flux Density (mJy)
	ASKAP		2019 Jun 16	984	0.887	1.002 ± 0.015
	VLA	20A-492	2020 Jun 6	1405	6	0.021 ± 0.008
	…	VLASS 2	2020 Sept 4	1485	3	<0.845
	…	21A-303	2021 Jun 14	1767	3	0.361 ± 0.076
	…	…	…	…	5	0.285 ± 0.013
	…	…	…	…	7	0.260 ± 0.009
	…	…	…	…	9	0.256 ± 0.010
	…	…	…	…	11	0.228 ± 0.009
	…	22B-205	2022 Nov 23	2291	1.25	<0.767
	…	…	…	…	1.75	0.193 ± 0.047
	…	…	…	…	3.0	0.210 ± 0.058
	…	…	…	…	6	0.163 ± 0.012
	…	…	…	…	10	0.089 ± 0.015
	…	…	…	…	15	0.086 ± 0.008
	…	…	…	…	20	0.053 ± 0.012
	…	…	…	…	24	0.039 ± 0.011
AT2018zr	VLA	20A-492	2020 Aug 23	929	6	<0.014
	VLA	21A-303	2021 Jun 18	1218	6	<0.053
	…	22B-205	2022 Oct 16	1713	6	0.147 ± 0.011
	…	…	2022 Dec 8	1743	1.25	<0.749
	…	…	…	…	1.75	0.218 ± 0.041
	…	…	…	…	2.5	0.209 ± 0.032
	…	…	…	…	3.5	0.180 ± 0.001
	…	…	…	…	5	0.155 ± 0.018
	…	…	…	…	7	0.109 ± 0.015
	…	…	…	…	9	0.088 ± 0.016
	…	…	…	…	11	0.085 ± 0.012
AT2020neh	VLA	22B-205	2022 Nov 9	874	6	0.026 ± 0.006
	…	…	2022 Dec 10	905	6	0.053 ± 0.012
AT2018dyb	MeerKAT	SCI-20210212-YC-01	2021 May 4	1028	1.36	0.158 ± 0.045
	MeerKAT	SCI-20220822-YC-01	2022 Dec 11	1615	1.36	1.031 ± 0.068
	ATCA	C3325	2023 Jan 22	1657	2.1	1.15 ± 0.07
	…	…	…	…	5.5	0.50 ± 0.04
	…	…	…	…	9	0.27 ± 0.03
AT2018hco	VLA	18A-373	2018 Dec 5	62	6	<0.0165
	…	VLASS 1	2019 May 5	213	3	<0.3
	…	21A-303	2021 June 12	982	6	0.343 ± 0.015
	…	VLASS 2	2021 Oct 14	1106	3	0.436 ± 0.142
	…	21B-360	2022 Jan 7	1191	1.5	<0.329
	…	…	…	…	2.5	0.166 ± 0.030
	…	…	…	…	3.5	0.252 ± 0.011
	…	…	…	…	5	0.265 ± 0.014
	…	…	…	…	7	0.227 ± 0.014
	…	…	…	…	9	0.161 ± 0.010
	…	…	…	…	11	0.371 ± 0.015
	ATCA	…	2022 Apr 30	1311	2.1	<0.33
	…	…	…	…	5.5	0.200 ± 0.019
	…	…	…	…	9	0.111 ± 0.019
	…	…	…	…	17	<0.084
	…	…	…	…	19	<0.141
	MeerKAT	SCI-20210212-YC-01	2022 May 7	1318	0.88	<0.589
	…	…	…	…	1.36	0.171 ± 0.025
AT2019ehz	VLA	VLASS 1	2017 Dec 1	−515	3	<0.39
	…	19A-395	2019 May 21	23	9	<0.06
	…	19A-395	2019 June 14	47	9	<0.026
	…	VLASS 2	2019 Sept 1	126	3	<0.3
	…	21A-303	2021 June 11	775	6	1.071 ± 0.032
	…	21B-360	2021 Dec 23	970	1.5	<0.237
	…	…	…	…	2.5	0.156 ± 0.070

Table 5
(Continued)

Object	Telescope	Project Code/ Source	Date of Observation	δt (days)	Frequency (GHz)	Flux Density (mJy)
	…	…	…	…	3.5	0.396 ± 0.046
	…	…	…	…	5	0.733 ± 0.041
	…	…	…	…	7	0.485 ± 0.059
	…	…	…	…	9	0.401 ± 0.014
	…	…	…	…	11	0.338 ± 0.015
	…	…	…	…	14	0.322 ± 0.015
	…	…	…	…	17	0.200 ± 0.012
	…	…	…	…	20	0.092 ± 0.016
	…	…	…	…	24	0.077 ± 0.014
	…	22B-205	2022 Oct 7	1262	1.5	<0.335
	…	…	…	…	2.5	0.245 ± 0.026
	…	…	…	…	3.5	0.309 ± 0.010
	…	…	…	…	5	0.205 ± 0.032
	…	…	…	…	7	0.235 ± 0.018
	…	…	…	…	9	0.184 ± 0.013
	…	…	…	…	11	0.111 ± 0.015
AT2019eve	VLA	VLASS 1	2017 Oct 28	−555	3	<0.3
	…	VLASS 2	2020 Oct 11	526	3	<0.497
	…	21A-303	2021 June 11	769	6	0.766 ± 0.009
	…	22B-360	2021 Dec 4	945	1.25	0.852 ± 0.120
	…	…	…	…	1.75	0.978 ± 0.053
	…	…	…	…	2.5	0.949 ± 0.039
	…	…	…	…	3.5	0.847 ± 0.020
	…	…	…	…	5	0.657 ± 0.022
	…	…	…	…	7	0.484 ± 0.024
	…	…	…	…	9	0.385 ± 0.034
	…	…	…	…	11	0.222 ± 0.023
	…	…	…	…	13.5	0.161 ± 0.023
	…	…	…	…	16.5	0.171 ± 0.015
	…	…	…	…	20	0.182 ± 0.011
	…	…	…	…	24	0.123 ± 0.012
	MeerKAT	DDT-20220414-YC-01	2022 May 5	1103	0.88	0.702 ± 0.040
	…	…	…	…	1.36	1.053 ± 0.020
	ATCA	C3472	2022 Apr 30	1092	2.1	0.770 ± 0.061
	…	…	…	…	5.5	0.543 ± 0.025
	…	…	…	…	9	0.300 ± 0.013
	…	…	…	…	17	0.122 ± 0.032
	…	…	…	…	19	<0.243
	…	22B-205	2022 Dec 19	1325	1.25	0.846 ± 0.175
	…	…	…	…	1.75	0.735 ± 0.048
	…	…	…	…	2.5	0.553 ± 0.028
	…	…	…	…	3.5	0.567 ± 0.018
	…	…	…	…	5	0.430 ± 0.020
	…	…	…	…	7	0.392 ± 0.015
	…	…	…	…	9	0.272 ± 0.019
	…	…	…	…	11	<6
	…	…	…	…	13.5	<4.2
	…	…	…	…	16.5	0.205 ± 0.010
	…	…	…	…	20	0.076 ± 0.020
	…	…	…	…	24	0.104 ± 0.016
	MeerKAT	SCI-20220822-YC-01	2023 Jan 4	1343	0.88	0.702 ± 0.040
AT2019teq	VLA	VLASS 2	2020 Aug 13	351	3	<0.329
	…	22B-205	2022 Oct 19	1096	6	0.238 ± 0.008
	…	…	2022 Dec 17	1155	1.25	0.492 ± 0.088
	…	…	…	…	1.75	0.430 ± 0.054
	…	…	…	…	2.5	0.283 ± 0.051
	…	…	…	…	3.5	0.268 ± 0.017
	…	…	…	…	5	0.159 ± 0.023
	…	…	…	…	7	0.064 ± 0.015
	…	…	…	…	9	<0.069

Table 5
(Continued)

Object	Telescope	Project Code/ Source	Date of Observation	δt (days)	Frequency (GHz)	Flux Density (mJy)
	…	…	…	…	11	0.046 ± 0.018
DES14C1kia	VLA	14B-506	2015 Jan 17	68	6	<0.017
	…	…	2015 Jan 17	68	21.7	<0.033
	…	…	2015 Mar 12	122	6	<0.015
	…	…	2015 Mar 12	122	21.7	<0.043
	VLA	20A-492	2020 May 28	2026	6	<0.013
iPTF15af	VLA	14A-483	2015 Jan 31	17	6.1	<0.084
	…	20A-492	2020 Jun 6	1970	6	<0.017
	…	22B-205	2022 Oct 25	2841	6	<0.008
iPTF16axa	VLA	21A-303	2021 Jun 17	1846	6	<0.011
	…	22B-205	2022 Oct 25	2841	6	<0.017
AT2017eqx	VLA	20A-492	2020 May 25	1090	6	<0.018
	…	22B-205	2022 Oct 7	1955	6	<0.011
AT2018fyk	MeerKAT	SCI-20210212-YC-01	2021 May 8	973	1.36	<0.060
	…	SCI-20220822-YC-01	2023 Jan 25	1601	1.36	<0.083
AT2018lna	VLA	21A-303	2021 Jun 20	906	6	<0.018
	…	22B-205	2022 Dec 8	1442	6	<0.012

Note. Upper limits are quoted as 3σ. This table only includes previously unpublished data for these TDEs; for published observations see Section 3.1.1. We note that the uncertainties listed in this table are statistical only and do not include an expected $\approx$3%–5% systematic uncertainty in the overall flux density calibration, which is taken into account in the equipartition analysis (Section 4.2).

(This table is available in machine-readable form in the online article.)

Table 6
All Other Radio Observations

Object	Telescope	Project Code/ Source	Date of Observation	δt (days)	Frequency (GHz)	Flux Density (mJy)
OGLE17aaj	ASKAP	VAST	2020 May 9	1224	1.42	<0.3
	…	…	2020 May 16	1230	1.42	<0.3
	…	…	2021 Apr 9	1391	1.42	<0.3
	MeerKAT	…	2021 May 1	1581	1.36	0.193 ± 0.020
	ATCA	C3472	2022 Apr 9	1924	2.1	<0.156
	…	…	…	…	5.5	<0.057
	…	…	…	…	9	<0.045
	…	…	…	…	17	<0.087
	…	…	…	…	19	<0.126
	MeerKAT	DDT-20220414-YC-01	2022 Apr 16	1931	0.82	0.290 ± 0.030
	…	…	…	…	1.36	0.215 ± 0.023
	…	SCI-20220822-YC-01	2022 Nov 24	2153	0.824	0.252 ± 0.05
	…	…	2022 Dec 3	2161	1.36	0.249 ± 0.023
	…	…	2023 Jan 5	2195	0.82	0.231 ± 0.025
AT2018bsi	VLA	21A-303	2021 Jun 20	1169	6	<0.013
	…	22B-205	2022 Dec 8	1705	6	0.037 ± 0.005
AT2018hyz	VLA	VLASS 3	2023 Feb 7	1578	3	16.838 ± 0.205
AT2020nov	VLA	20A-372	2020 Oct 16	111	15	0.224 ± 0.009
	…	…	2021 Feb 10	228	6	0.376 ± 0.010
	…	…	2021 Feb 28	246	6	0.370 ± 0.010
	VLA	22B-205	2022 Nov 13	869	6	0.366 ± 0.019
AT2020mot	VLA	22B-205	2022 Nov 18	887	6	0.086 ± 0.008
AT2020pj	VLA	VLASS 1	2020 Sept 19	261	3	<0.465
	…	22B-205	2022 Oct 28	1030	6	0.118 ± 0.006

Table 6
(Continued)

Object	Telescope	Project Code/ Source	Date of Observation	δt (days)	Frequency (GHz)	Flux Density (mJy)
	⋯	⋯	2022 Dec 15	1078	6	0.093 ± 0.011
	⋯	VLASS 2	2023 Jan 24	1118	3	<0.454
AT2020wey	VLA	20A-372	2020 Oct 30	22	15	<0.014
	⋯	⋯	2021 Feb 13	128	6	0.0408 ± 0.081
	⋯	22B-205	2022 Oct 7	729	6	<0.018

Note. Upper limits are quoted as 3σ. We note that the uncertainties listed in this table are statistical only and do not include an expected ≈3%–5% systematic uncertainty in the overall flux density calibration, which is taken into account in the equipartition analysis (Section 4.2).

(This table is available in machine-readable form in the online article.)

ORCID iDs

Y. Cendes https://orcid.org/0000-0001-7007-6295
E. Berger https://orcid.org/0000-0002-9392-9681
K. D. Alexander https://orcid.org/0000-0002-8297-2473
R. Chornock https://orcid.org/0000-0002-7706-5668
R. Margutti https://orcid.org/0000-0003-4768-7586
B. Metzger https://orcid.org/0000-0002-4670-7509
M. H. Wieringa https://orcid.org/0000-0002-7721-8660
M. F. Bietenholz https://orcid.org/0000-0002-0592-4152
A. Hajela https://orcid.org/0000-0003-2349-101X
T. Laskar https://orcid.org/0000-0003-1792-2338
M. C. Stroh https://orcid.org/0000-0002-3019-4577
G. Terreran https://orcid.org/0000-0003-0794-5982

References

Alexander, K. D., Berger, E., Guillochon, J., Zauderer, B. A., & Williams, P. K. G. 2016, ApJL, 819, L25
Alexander, K. D., van Velzen, S., Horesh, A., & Zauderer, B. A. 2020, SSRv, 216, 81
Andreoni, I., Coughlin, M. W., Perley, D. A., et al. 2022, Natur, 612, 430
Angus, C. R., Baldassare, V. F., Mockler, B., et al. 2022, NatAs, 6, 1452
Baganoff, F. K., Maeda, Y., Morris, M., et al. 2003, ApJ, 591, 891
Barniol Duran, R., Nakar, E., & Piran, T. 2013, ApJ, 772, 78
Beniamini, P., Piran, T., & Matsumoto, T. 2023, MNRAS, 524, 1386
Berger, E., Zauderer, A., Pooley, G. G., et al. 2012, ApJ, 748, 36
Blagorodnova, N., Cenko, S. B., Kulkarni, S. R., et al. 2019, ApJ, 873, 92
Blagorodnova, N., Gezari, S., Hung, T., et al. 2017, ApJ, 844, 46
Blanchard, P. K., Nicholl, M., Berger, E., et al. 2017, ApJ, 843, 106
Brown, G. C., Levan, A. J., Stanway, E. R., et al. 2015, MNRAS, 452, 4297
Brown, G. C., Levan, A. J., Stanway, E. R., et al. 2017, MNRAS, 472, 4469
Cendes, Y., Alexander, K., Berger, E., et al. 2022a, ATel, 15728, 1
Cendes, Y., Alexander, K. D., Berger, E., et al. 2021a, ApJ, 919, 127
Cendes, Y., Berger, E., Alexander, K. D., et al. 2022b, ApJ, 938, 28
Cendes, Y., Eftekhari, T., Berger, E., & Polisensky, E. 2021b, ApJ, 908, 125
Cenko, S. B., Krimm, H. A., Horesh, A., et al. 2012, ApJ, 753, 77
Chandra, P., Stockdale, C. J., Chevalier, R. A., et al. 2009, ApJ, 690, 1839
Christy, C. T., Alexander, K. D., & Cendes, Y. 2024, arXiv:2404.12431
Condon, J. J., Cotton, W. D., Greisen, E. W., et al. 1998, AJ, 115, 1693
Coughlin, E. R., & Begelman, M. C. 2014, ApJ, 797, 103
De Colle, F., Guillochon, J., Naiman, J., & Ramirez-Ruiz, E. 2012, ApJ, 760, 103
Eftekhari, T., Berger, E., Zauderer, B. A., Margutti, R., & Alexander, K. D. 2018, ApJ, 854, 86
Foley, R. J., Blanchard, P. K., Challis, P., et al. 2015, ATel, 6877, 1
Foreman-Mackey, D., Hogg, D. W., Lang, D., & Goodman, J. 2013, PASP, 125, 306
Frederick, S., Gezari, S., Velzen, S. V., et al. 2020, TNSAN, 143, 1
Giannios, D., & Metzger, B. D. 2011, MNRAS, 416, 2102
Gillessen, S., Plewa, P. M., Widmann, F., et al. 2019, ApJ, 871, 126
Gomez, S., Nicholl, M., Short, P., et al. 2020, MNRAS, 497, 1925
Goodwin, A., Miller-Jones, J., Alexander, K. D., et al. 2023a, ATel, 16165, 1
Goodwin, A. J., Alexander, K. D., Miller-Jones, J. C. A., et al. 2023b, MNRAS, 522, 5084
Goodwin, A. J., Miller-Jones, J. C. A., van Velzen, S., et al. 2023c, MNRAS, 518, 847
Goodwin, A. J., van Velzen, S., Miller-Jones, J. C. A., et al. 2022, MNRAS, 511, 5328
Granot, J., & Sari, R. 2002, ApJ, 568, 820
Gromadzki, M., Hamanowicz, A., Wyrzykowski, L., et al. 2019, A&A, 622, L2
Guillochon, J., & Ramirez-Ruiz, E. 2013, ApJ, 767, 25
Hammerstein, E., van Velzen, S., Gezari, S., et al. 2023, ApJ, 942, 9
Hayasaki, K., & Jonker, P. G. 2021, ApJ, 921, 20
Heywood, I. 2020, oxkat: Semi-automated Imaging of MeerKAT Observations, Astrophysics Source Code Library, ascl:2009.003
Holoien, T. W. S., Auchettl, K., Tucker, M. A., et al. 2020, ApJ, 898, 161
Holoien, T. W. S., Prieto, J. L., Bersier, D., et al. 2014, MNRAS, 445, 3263
Horesh, A., Cenko, S. B., & Arcavi, I. 2021a, NatAs, 5, 491
Horesh, A., Sfaradi, I., Bright, J., et al. 2018, ATel, 12271, 1
Horesh, A., Sfaradi, I., Fender, R., et al. 2021b, ApJL, 920, L5
Hung, T., Cenko, S. B., Roth, N., et al. 2019, ApJ, 879, 119
Hung, T., Gezari, S., Blagorodnova, N., et al. 2017, ApJ, 842, 29
Irwin, J. A., Henriksen, R. N., Krause, M., et al. 2015, ApJ, 809, 172
Jiang, N., Wang, T., Yan, L., et al. 2017, ApJ, 850, 63
Lacy, M., Baum, S. A., Chandler, C. J., et al. 2020, PASP, 132, 035001
Leloudas, G., Dai, L., Arcavi, I., et al. 2019, ApJ, 887, 218
Liodakis, I., Koljonen, K. I. I., Blinov, D., et al. 2023, Sci, 380, 656
Loeb, A., & Ulmer, A. 1997, ApJ, 489, 573
Matsumoto, T., & Piran, T. 2023, MNRAS, 522, 4565
McMullin, J. P., Waters, B., Schiebel, D., Young, W., & Golap, K. 2007, in ASP Conf. Ser. 376, Astronomical Data Analysis Software and Systems XVI, ed. R. A. Shaw, F. Hill, & D. J. Bell (San Francisco, CA: ASP), 127
Metzger, B. D. 2022, ApJL, 937, L12
Metzger, B. D., Giannios, D., & Mimica, P. 2012, MNRAS, 420, 3528
Murphy, T., Kaplan, D. L., Stewart, A. J., et al. 2021, PASA, 38, e054
Nakar, E., & Piran, T. 2011, Natur, 478, 82
Nicholl, M., Blanchard, P. K., Berger, E., et al. 2019, MNRAS, 488, 1878
Nicholl, M., Wevers, T., Oates, S. R., et al. 2020, MNRAS, 499, 482
O'Brien, A., Kaplan, D., Murphy, T., Yu, W., & Zhang, W. 2019, ATel, 13310, 1
Pasham, D. R., & van Velzen, S. 2018, ApJ, 856, 1
Perlman, E. S., Meyer, E. T., Wang, Q. D., et al. 2022, ApJ, 925, 143
Petrushevska, T., Leloudas, G., Ilić, D., et al. 2023, A&A, 669, A140
Russell, H. R., Fabian, A. C., McNamara, B. R., & Broderick, A. E. 2015, MNRAS, 451, 588
Sari, R., Piran, T., & Narayan, R. 1998, ApJL, 497, L17
Sfaradi, I., Beniamini, P., Horesh, A., et al. 2024, MNRAS, 527, 7672
Sfaradi, I., Horesh, A., Fender, R., et al. 2022, ApJ, 933, 176
Short, P., Nicholl, M., Lawrence, A., et al. 2020, MNRAS, 498, 4119
Stein, R., van Velzen, S., Kowalski, M., et al. 2021, NatAs, 5, 510
Stone, N., Sari, R., & Loeb, A. 2013, MNRAS, 435, 1809

Teboul, O., & Metzger, B. D. 2023, ApJL, 957, L9
van Velzen, S. 2018, ApJ, 852, 72
van Velzen, S., Gezari, S., Cenko, S. B., et al. 2019, ApJ, 872, 198
van Velzen, S., Gezari, S., Hammerstein, E., et al. 2021, ApJ, 908, 4
van Velzen, S., Holoien, T. W. S., Onori, F., Hung, T., & Arcavi, I. 2020, SSRv, 216, 124
Wevers, T., Pasham, D. R., van Velzen, S., et al. 2019, MNRAS, 488, 4816
Williams, P. K. G., Gizis, J. E., & Berger, E. 2017, ApJ, 834, 117
Wright, E. L. 2006, PASP, 118, 1711
Yao, Y., Ravi, V., Gezari, S., et al. 2023, ApJL, 955, L6
Zauderer, B. A., Berger, E., Margutti, R., et al. 2013, ApJ, 767, 152
Zauderer, B. A., Berger, E., Soderberg, A. M., et al. 2011, Natur, 476, 425